EXPERIMENTAL STUDIES OF THE HEAT TRANSFER CHARACTERISTICS OF SILICA NANOPARTICLE WATER-BASED DISPERSION IN POOL BOILING USING NICHROME FLAT RIBBONS AND WIRES

by

DIANE MARIE VAZQUEZ
B.S.M.E. University of Central Florida, 2008

A thesis submitted in partial fulfillment of the requirements
for the degree of Master of Science in Mechanical Engineering
in the Department of Mechanical, Materials, and Aerospace Engineering
in the College of Engineering and Computer Science
at the University of Central Florida
Orlando, Florida

Spring Term
2010

ABSTRACT

This work deals with a study of enhanced critical heat flux (CHF) and burnout heat flux (BHF) in pool boiling of water with suspended silica nanoparticles using ribbon-type and wire heaters. Previously our group and other researchers have reported three-digit percentage increase in critical heat flux in silica nanofluids. This study investigates the effect of various heater surface dimensions and cross-sectional shapes on pool boiling heat transfer characteristics of water and water-based nanofluids. CHF and BHF were analyzed for circular and rectangular cross-section nichrome wires and ribbons of increasing sizes in the range of 0.32mm to 2.38mm width, approaching a flat-plate scenario. Experimental trends showed that the CHF and BHF in water pool boiling decrease as heater surface area increases, and for similar surface area, the wire had a 25% higher CHF than that of the ribbon. For concentrations from 0.1vol% to 2vol%, various properties such as viscosity, pH, and surface tension as well as silica deposition on surface and glowing length of ribbon were measured in order to study the possible factors in the heat transfer behavior of nanofluids. The deposition of the particles on the wire allows high heat transfer through inter-agglomerate pores, resulting in a nearly 3-fold increase in burnout heat flux at very low concentrations. Results have shown a maximum of up to 340% CHF enhancement for ribbon-type heaters, and the relationship of CHF with respect to nanoparticle concentration has been found to be non-monotonic with a peak around 0.2vol% to 0.4vol%. Visualization of boiling experiments aided with determination of relative bubble sizes, nucleation, and flow regimes. The surface morphology of the heater was investigated using SEM and EDS analyses, and it was inferred that the 2vol% concentration deposition coating had higher porosity and rate of deposition compared with 0.2vol% case.

To my parents,

Edith and Domingo Vazquez,

for instilling in me the passion for learning,

for their constant encouragement and unconditional love.

ACKNOWLEDGMENTS

I would like to express my sincerest gratitude to my research advisor Dr. Ranganathan Kumar for his support and guidance throughout the course of this project and for enabling me to become a better researcher. I thank him for allowing me to do experimental work in this interesting, emerging field that encompasses nanofluids. I appreciate his financial support in my graduate studies at UCF and for the opportunity to further my knowledge in Mechanical Engineering. I thank my thesis committee members Dr. Louis Chow and Dr. Saptarshi Basu for their insightful questions and comments regarding this work and for the invaluable knowledge I gained in the courses I took under them. I also thank Dr. Sohel Murshed for the helpful discussions about my project and for his advice on my research. I appreciate the assistance offered by Mr. Kirk Scammon, Research Engineer at the Materials Characterization Facility, AMPAC at UCF, in obtaining the SEM images and EDS data. I gratefully acknowledge the financial support provided by the College of Graduate Studies through the UCF Provost's Graduate Fellowship.

I am deeply grateful for my parents who have guided and encouraged me throughout my whole life and have given me impetus to pursue my dreams. I treasure the values they imparted to me which have formed my mindset and have taught me to do everything with excellence as unto the Lord. I also thank my sister and brother-in-law who have been of loving encouragement in all my studies and my role models in life. My deep appreciation is extended to my dear family and friends whose love and support in all my endeavors have been heartening to me.

Most importantly, I thank my Lord and Savior Jesus Christ, who has continually given me divine wisdom and guidance in life, who is my ultimate inspiration, and without whom the completion of this project would not have become a reality.

TABLE OF CONTENTS

LIST OF FIGURES

LIST OF TABLES

LIST OF NOMENCLATURE

BHF	Burnout Heat Flux, kW/m^2
BSE	Backscatter Electron
CHF	Critical Heat Flux, kW/m^2
D	Diameter of wire, mm
DI	Deionized
DNB	Departure from Nucleate Boiling
EDS	Energy Dispersive X-ray Spectroscopy
h	Height of deposition on one side, μm
I	Current, A
L	Length of wire/ribbon, mm
ONB	Onset of Nucleate Boiling
q"	Heat Flux, kW/m^2
R	Resistance, Ω
SE	Secondary Electron
SEM	Scanning Electron Microscope
t	Thickness of ribbon, mm
T_{sat}	Saturation Temperature °C
T_w	Temperature at wall/surface of heated element, °C
$T_w - T_{sat}$	Wall Superheat or Excess Temperature, °C
V	Voltage, V
W	Width of ribbon, mm
μ	Dynamic viscosity, cP
σ	Surface tension, mN/m
φ	Concentration, vol%

CHAPTER ONE: INTRODUCTION

Nanoparticles Overview

Argonne National Laboratory utilized modern nanotechnologies to process and manufacture nanometer-sized particles with average crystallite sizes below 50 nm. The suspension of these metallic or non-metallic particles in a base fluid (water, oil, or ethylene glycol) was then termed nanofluid, and this new concept is considered a new class of heat transfer fluid, as they have been found to transfer heat more efficiently than conventional fluids [1]. The advantage of nanoparticles is the extremely large surface-area-to-volume ratio, which offers great potential in heat transfer applications since heat transfer takes place at the surface of the particle. For instance, the surface-area-to-volume ratio of a 10nm-diameter particle is 1000 times that of a conventional, 10μm-diameter particle. Nanoparticles also offer better performance than conventional particles because they provide a more stable suspension, with little settling even after weeks or months and little agglomeration. Additionally, the small size of these particles facilitate their usage for minichannels and microchannels, where the micro- and millimeter particles have a tendency to clog the channels. With modern technologies giving rise to high-operating-temperature systems and small devices, there is a need for better coolants that can extend the life and range of the components so as not to compromise the functional and structural integrity of the system. Thus, these nanofluids have promising potential applications in electronic cooling, heat exchangers, optical systems, and microchannels.

The Boiling Phenomenon and Critical Heat Flux Mechanisms

Boiling is a naturally occuring phenomenon in fluids in which there is a phase change from the liquid phase to the gaseous phase at a certain system pressure and temperature. In hetergeneous nucleation, a vapor bubble forms at and grows from a nucleation site on a heated surface when the wall temperature reaches a certain superheat above the saturation temperature at the system pressure. Boiling is an effective means of carrying away heat from a heated surface; therefore, it is used as a method for cooling heated systems. As materials and systems become more sophisticated and can attain higher operating temperatures, a common goal of researchers is to find ways to enhance the heat transfer from the heated surface into the liquid and to understand the underlying physics of such enhancements. The focus of this work is the topic of pool boiling – boiling from a surface in a largely quiesent fluid.

Nukiyama [2] was a pioneer in boiling heat transfer, leading investigations in pool boiling, establishing the boiling curve, and being among the first to describe the events in the various boiling regimes. In the first boiling regime, natural convection, low wall superheats cause a thermal gradient in the locally surrounding liquid allowing for convection in the liquid pool due to differences in densities; however, boiling does not occur since the superheat is not large enough to cause vapor pressure to overcome bubble surface tension. The incipience of boiling occurs at the termed onset of nucleate boiling (ONB) point. In the regime of nucleate boiling there are two major physical mechanisms that govern the thermal transport: 1) latent heat of vaporization, where superheated liquid is vaporized, carrying away with it heat energy from the surface, and 2) dryout of the heater surface. These two mechanisms work against each other in

the overall purpose of effectively carrying heat away from the surface and thus, delaying the critical failure of the heater element in the pool boiling scenario. As the wall superheat is increased in the nucleate boiling regime, the number of active nucleation sites increases and the frequency of the isolated bubbles increases. The spacing between the nucleation sites becomes closer, causing the bubbles to coalesce, and with the bubbles rising so quickly, this creates a column of vapor slugs. In the higher heat flux range of the nucleate boiling regime (the regime of slugs and columns), the amount of vapor produced near the heater increases to such an extent that the liquid is increasingly unable to wet the surface, thus creating the gradual dryout of the surface and the onset of the critical heat flux (CHF) condition. This is the general concensus in the literature; although, several theories have been postulated for the departure from nucleate boiling (DNB), three of which are summarized below.

The hydrodynamic instability theory [3] postulates that the high velocity of the vapor rising creates an instability with the slower, descending liquid, creating a distorted column of vapor and interrupting the liquid flow to the heater surface. The decreasing amount of liquid that reaches the surface is vaporized, leading to the blanketing of vapor and CHF. Another theory [4] explains that dry spots are formed over hot portions of the surface and are subsequently rewet axially upon bubble departure. DNB occurs when the horizontal force of the vapor is greater than the liquid vapor surface tension, causing the liquid to further receed and finally dry out the surface. Still another theory [5] proposes that at high heat flux a vapor plume or mushroom hovers above the surface, being fed underneath by numerous vapor feeder jets rising from the surface. The feeder jet develops from an individual nucleation site when the rate of vaporization

is so high that a continuous jet of vapor rises. A layer of liquid, termed the macrolayer, separates the large vapor bubble from the surface and is trapped in between the feeder jets. DNB is said to occur when this macrolayer is depleted or when the hovering time is greater than the time required to dry out the macrolayer.

The theoretical background of the experimental system of the present work is based on the design of Nukiyama's [2] experiment, which was the first of its kind to implement a controlled heat flux scenario in pool boiling by passing current through a wire and measuring the voltage to obtain the wire temperature. Of particular concern in this investigation is the CHF of the heater element which is of great importance to its functional life. This is the heating point at which additional heating causes a sudden increase in temperature, glowing of the heater element, and eventual burnout of the heater (controlled heat flux case). For the usefulness of a heater in practical application, it is essential to remain well below the critical heat flux, so the objective in boiling heat transfer is to enhance the boiling performance and CHF.

The objective of this work is to experimentally investigate the effect of various heater surface dimensions and cross-sectional shapes on pool boiling heat transfer in water and to study the effects of various parameters and characteristics on CHF and BHF as a function of nanoparticle concentration in order to be able to provide further insight into the sources of the observed boiling heat transfer enhancement as a result of nanofluid pool boiling.

CHAPTER TWO: LITERATURE REVIEW

Critical Heat Flux Enhancement and Parametric Effects

Vassallo et al. [6] and Milanova and Kumar [7] have shown a CHF enhancement of ~200% for 0.5vol% silica (SiO_2) nanofluids on wire heaters. Kim et al. [8] conducted experiments with titania (TiO_2) and alumina (Al_2O_3) ranging from 10^{-5}vol% to 10^{-1}vol% concentrations. They found a ~100% CHF enhancement for pool boiling of titania and alumina nanofluids on nichrome wires and saw nanoparticle deposition on the wire heaters. They also studied pool boiling of pure water on nanoparticle-deposited wires and found that the CHF enhancements were not less high than those of nanofluids. You et al. [9] reported a ~200% enhancement for alumina on a copper flat plate. Bang and Chang [10] experimented with 0.5vol% to 4vol% alumina nanofluid, and found ~50% and ~13% CHF enhancement for 1vol% alumina on a horizontal and vertical plate, respectively. Kim et al. [11] employed alumina, zirconia (ZrO_2), and silica (0.001vol% - 0.1vol%) nanofluids in pool boiling of wire heater and found CHF enhancements of 52%, 75%, and 80%, respectively. Wu et al. [12] used a copper plate with 1μm-thick coatings of TiO_2 nanoparticles and SiO_2 nanoparticles of 10nm size. In water pool boiling experiments they found that the TiO_2 coated surface showed a 50.4% CHF enhancement, and the SiO_2 coated surface a 10.7% CHF enhancement.

According to the Zuber [3] model based on Taylor wave motion and Helmholtz instability derived from hydrodynamic theory in the critical boiling stage, the correlation for maximum heat flux for an infinite flat plate is

$$q"_{max} = 0.131\rho_v h_{lv}\left[\frac{\sigma(\rho_l-\rho_v)g}{\rho_v^2}\right]^{1/4} \quad (1)$$

where ρ_v and ρ_l are the vapor and liquid densities; and h_{lv}, σ, and g are the latent heat of vaporization, surface tension, and gravity, respectively. With numerous results in literature showing an enhancement in CHF due to a small concentration of nanoparticles and a minimal change in fluid properties, Zuber's correlation alone cannot explain such a high increase in CHF because the correlation depends only on the fluid properties. This has led researchers to explore and study the effect of various other parameters to determine the cause of CHF enhancement due to nanoparticles. Studies have shown that parameters such as heater geometry [13], [14], surface roughness, heater thermal properties [15], [16], three-phase contact angle, and wettability of fluid/surface combination have been shown to affect nucleate boiling and ultimately CHF. Interestingly, a common result that has been seen in nanofluid pool boiling is nanoparticle surface coating (deposition), which incorporates several of these physical parameters. This nanoparticle deposition has been proposed to be the main factor in the enhancement of pool boiling CHF in nanofluids [8], [17]. As an example, in Figure 1 SEM images taken by Kim and Kim [18] show the structures of titania, silica, and silver nanoparticles deposited on a wire after boiling, as well as a bare nichrome wire.

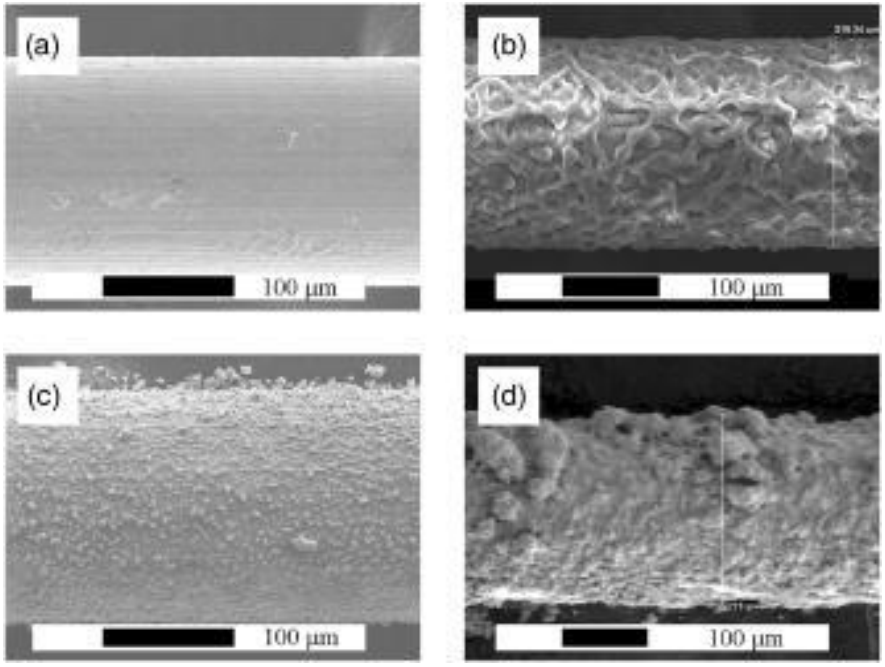

Figure 1: Scanning electron micrographs, a) bare nichrome wire, b) nanoparticle-deposited wire produced during pool boiling of water-based nanofluids containing titania, c) silica, d) silver (Ag) nanoparticles with a 0.1vol% concentration [18].

Furthermore, an interesting experimental study was done by Forrest et al. [19] in which a layer-by-layer (LbL) technique was implemented to coat a nickel substrate with a thin film (up to 1μm) composed of silica nanoparticles. The superhydrophilic surface pool boiled in pure water showed a 101% CHF enhancement over that of a clean surface in water boiling. They conjecture that CHF enhancement can be caused by nanoscale surface modifications – the nanoporous nature of the coatings – affecting the surface wettability, chemical constituency and total pore volume dependent on coating thickness. Additionally, they reported no change in surface roughness due to the coating.

Effect of Surface Roughness on CHF

In some studies, surface roughness has been shown to increase as a result of the nanoparticle layer on the surface, directly increasing the effective surface area, and this has been shown to enhance boiling performance [12], [20]. Surface roughness images taken by Kim et al. [11] via a profilometer are shown in Figure 2, which gives a comparison of a stainless steel surface after boiling water and 0.01vol% alumina nanofluid. It can be seen that the boiling of nanofluid indeed caused an increase in surface roughness. Yet, there are conflicting results in the literature [6], [9], [10], [11], [21] regarding the negative or neutral effects of surface roughness on boiling heat transfer. The variation of surface roughness of the plain surfaces along with variation in particle size from study to study can greatly affect the underlying physics due to nanoparticles possibly filling in larger surface imperfections; therefore, boiling heat transfer performance data can vary. Nevertheless, the aforementioned studies showed significant increase in CHF. Kim et al. [22] comment that the effects of roughness on CHF were not easily determined in their study, since the surface has a "very complex and fractal geometry with micro and nano scales in hierarchical surface topography." They offer that since surface roughness can control the degree of wettability, they claim that the wettability of the coated surface must have been amplified by its complex geometry, which may tremendously affect CHF enhancement. It seems as though surface roughness alone cannot determine the nucleate boiling heat transfer behavior; however, it is certain that changing roughness affects surface characteristics, such as the apparent contact angle [23].

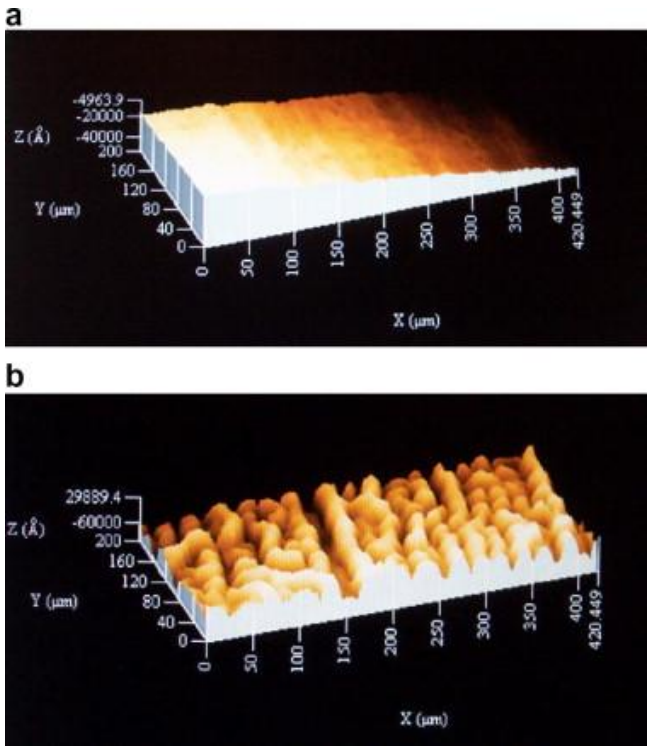

Figure 2: Profilometer images of stainless steel 316 after boiling: a) pure water, rms roughness ~0.1µm, b) 0.01vol% alumina, rms roughness ~2µm [11].

Effect of Contact Angle on CHF

A more important parameter that has been investigated is the contact angle in which surface roughness plays a role through the equation

$$\cos\theta = \frac{\gamma_{SV} - \gamma_{SL}}{\sigma} r \tag{2}$$

where θ is the static contact angle, γ_{SV} is the solid-vapor interfacial tension, γ_{SL} is the solid-liquid interfacial tension ($\gamma_{SV} - \gamma_{SL}$ is the adhesion tension), σ is the liquid-vapor surface tension, and r is a roughness factor (ratio of effective contact area to smooth contact area) [11]. Reduction in three-phase contact angle (increased wettability of a surface) due to nanoparticle-deposited

surfaces has been shown to have a positive correlation with enhancement of CHF [7], [11], [24], [25], [26], [27]. Kim et al. [11] report that the contact angle of a water droplet on a nanosilica-boiled surface ranged from 8°-18°, and for 0.1vol% silica nanofluid droplet on nanosilica-coated surface the angle was 21°, both much less than the nominal angle of water on a clean metal surface ~80°. Figure 3 shows contact angle results for combinations of pure water and alumina droplets on clean and deposited surfaces, and the lowest contact angles (22°, 23°) resulted from the nanoparticle-deposited surfaces.

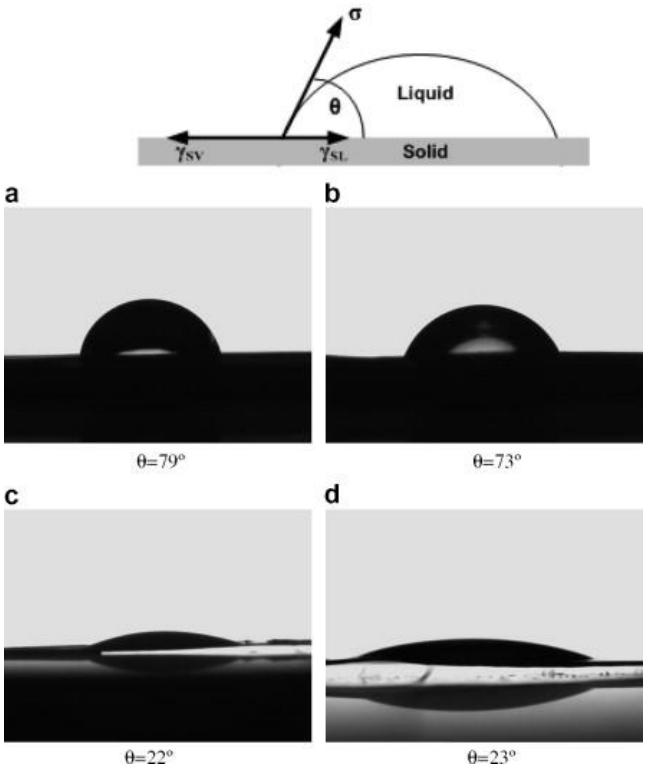

Figure 3: Static contact angles of 5µL sessile droplets on stainless steel surfaces, a) pure water droplet on water-boiled surface, b) 0.01vol% alumina droplet on water-boiled surface, c) pure water droplet on 0.01vol% alumina-boiled surface, d) 0.01vol% alumina droplet on 0.01vol% alumina-boiled surface [11].

From a theoretical approach, Kirichenko and Chernyakov [28] developed the following correlation via an extension of the hydrodynamic instability theory at CHF, incorporating the contact angle β:

$$q"_{max} = 0.171 h_{lv}\sqrt{\rho_v}[\sigma g(\rho_l - \rho_v)]^{1/4} \frac{(1+0.324*10^{-3}\beta^2)^{1/4}}{\sqrt{0.018\beta}}. \quad (3)$$

It is important to note that the contact angle considered in the above experimental results and correlation was the static contact angle, whereas the real boiling scenario is dictated by the dynamic receding contact angle. This parameter is inherently more difficult to measure and is slightly different than the static contact angle, but trends from the aforementioned analyses show that as the contact angle decreases, the CHF increases.

Effect of Capillary Wicking on CHF

Kim and Kim [18] proposed that capillary wicking through the porous layer causes the cooler fluid to reach and wet the heater surface, thus delaying the onset of critical condtition due to rewetting of a dry spot in bubble growth. Figure 4 shows a representation of the capillary wicking that occurs through the porous layer. In a study by Kim et al. [22], they investigated liquid spreadability by measuring the amount a water droplet spread in one second on a flat surface which had grown ZnO nanorods of 800-900nm height .They found that the nanorod-covered surface showed rapid liquid spreading and suggest that spreadability may be related to the "good liquid adhesion arising from the highly wettable nature of nanorods structures and the excellent water spreading condition due to a morphology that facilitates capillary action," which is an important contributor to CHF enhancement. In another study, it is suggested that capillary

wicking through the micro-flow-passes creates a thin film of cooler fluid covering the particles, and evaporation of this thin film on the increased effective boiling surface area contributes to the enhanced boiling heat transfer [29].

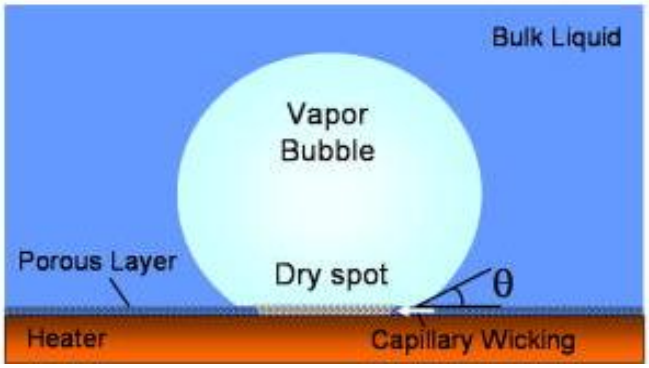

Figure 4: Capillary wicking rewetting a dry spot of vapor bubble growth [18].

Effect of Fouling on CHF

Although it has been seen in various research studies that deposition plays a major role in the enhancement of CHF of pool boiling, there may arise opposing effects to the CHF enhancement with continued increase in deposition thickness. Coursey et al. [26] state that an improved surface wettability due to deposition may be negated by another mechanism such as fouling. Therefore, there may be a limit where increasing the nanoparticle concentration above a certain threshold could impose a neutral or detrimental effect on the CHF enhancement. Clearly, more research needs to be done in this area to fully understand the effect of nanofluids in pool boiling.

Effect of Thermal Conductivity

The effect of nanoparticles on thermophysical properties, such as thermal conductivity, of the nanofluid has been a topic of debate among research groups. The colloidal dispersion of nanoparticles within an aqueous matrix brings about complexities in the understanding of heat propagation through the medium. It further obscures the heat transfer behavior and hydrodynamics of the boiling problem. Thus, studies have been done to assess the impact of nanoparticles on thermal conductivity by performing measurements at moderate temperatures. A semi-blind benchmark study named INPBE International Nanofluid Property Benchmark Exercise [30] was performed by 30 organizations worldwide, in which they measured thermal conductivity of identical samples of nanofluids. All results were compared, and the water-based data from most groups deviated from the sample average by ±5% or less and agreed well with current theoretical predictions. Table 1 shows measured thermal conductivity ratios of alumina and silica nanofluid with respect to the base fluid DI water. Alumina thermal conductivity enhancement was 3.6% for 1vol%, and silica was 20.4% for 31vol%. They found that for low concentrations, conductivity enhancement was low but increased with increasing concentration.

Table 1: Results (partial) from benchmark study measuring thermal conductivity ratio of nanofluid to base fluid DI water [30].

Particle	Particle size	Concentration	k_{nf}/k_f
Alumina nanorods	80 x 10nm^2	1vol% in DI water	1.036±0.004
Silica nanoparticles	22nm	31vol% in DI water + stabilizer	1.204±0.010

CHAPTER THREE: METHODOLOGY

Experimental Setup

The experimental setup as shown in Figure 5 consists of 30 Amp DC power supply (Kenwood, PD 18-30AD), heater plate (Fisher Scientific), Pyrex glass cylindrical test section, 10mm-thick acrylic cover, coiled double jacketed condenser, multimeter (Agilent, 34401A), data acquisition system (DAQ), and type K thermocouple. Similar to previous work [31], the experimental procedure involves passing current through nichrome 80/20 wire or ribbon, which serves as the heater element and a temperature sensor simultaneously. Soldered to the nichrome metal are copper lead wires and voltage sense wires leading to a multimeter. The current work uses a nichrome ribbon which is oriented horizontally as shown in the inset of Figure 5. The heater circuit assembly is submerged in a pool of approximately 200 mL of sample fluid in the glass test section and is subsequently heated on the plate to the saturation temperature T_{sat} (100°C) at atmospheric pressure, with bulk temperature monitored by the thermocouple. The current is regulated through the DAQ system in this experiment for constant heat flux control, with an initial value of 0.2A (minimal current not affecting wire heating), and it is increased at 0.1A increments every 3 seconds. The voltage measurements are taken through the DAQ system 0.1s after the current increase, to allow time to equilibrate. The heat flux is calculated by using the equation

$$q'' = (I\ V) / (P\ L) \tag{4}$$

where I is the current input, V is the measured potential drop, P is the perimeter of the cross-section of the wire/ribbon, and L is the length of the nichrome between the voltage sense wires

(~40mm). Ohm's law (V=I.R) is used to find the temperature of the nichrome ribbon wire, T_w, by obtaining the resistance R of the ribbon and then using a temperature-resistance calibration curve, as discussed further later. The pool boiling curve, heat flux versus wall superheat ($T_w - T_{sat}$), is then generated with the acquired data and comparisons are made among the various heater geometries and nanoparticle concentrations.

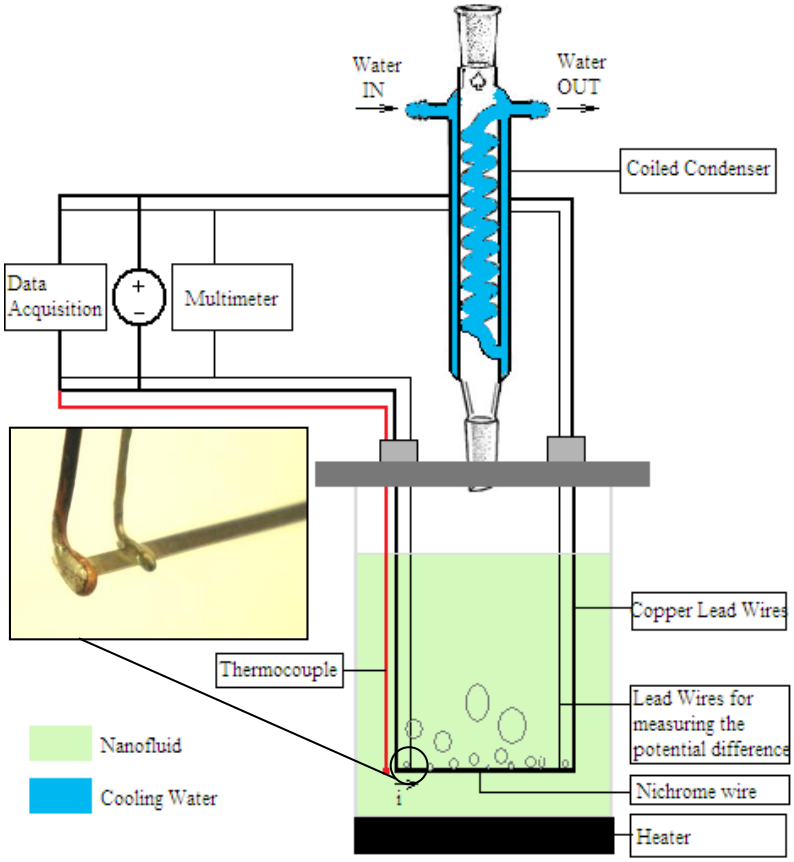

Figure 5: Pool Boiling Experimental Setup.

Deposition thickness was measured with calipers at 5 equidistant locations along each nichrome heater that was used, and error bars represent the standard deviation of the variation of deposition on each wire and repeated runs. Additionally, visualization of the pool boiling experiments was

implemented with a high-speed digital camera (Canon Rebel XT) to aid in conceptual understanding and bubble and glowing length measurements.

Experimental studies of DI water pool boiling were done on several sizes of nichrome cylindrical wires and rectangular ribbons to find out the impact of shape on the boiling heat transfer behavior. Table 2 shows the types of heaters used and the convective surface area based on an average length of 40mm for each heater.

Table 2: Cylindrical wires and rectangular ribbons used in experiments and respective surface area.

Size Wire/Ribbon	**Surface Area [mm^2]**
0.32mm Diameter Wire	40.22
0.4 x 0.127mm Ribbon	41.91
0.4mm Diameter Wire	50.75
0.79 x 0.127mm Ribbon	73.66
1.59 x 0.127mm Ribbon	137.16
2.38 x 0.127mm Ribbon	200.66

Calibration

The temperature-resistance calibration curve (Figure 6) is given as a resistance factor of the temperature by the manufacturer [32]. In the low temperature region the temperature was seen to be over-predicted for the present experiments; therefore, for the range of 100°C to 150°C, an in situ calibration was done as described in [31] and the resulting correlation can be seen in Figure 6 inset.

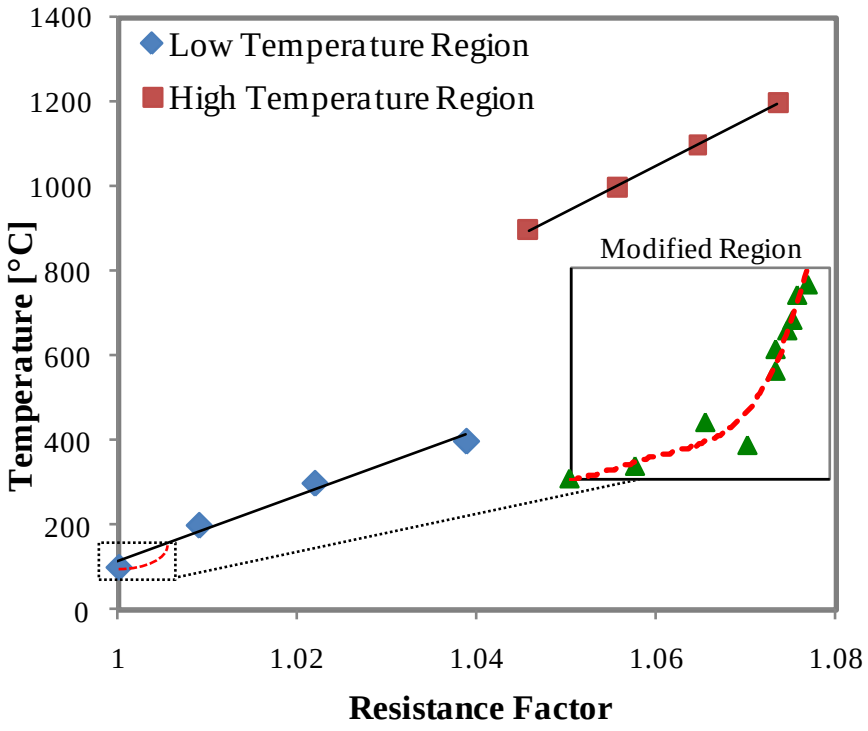

Figure 6: Temperature-resistance curve with modified region (inset).

Uncertainty in the heat flux calculations can be attributed to instrument errors, random errors and inherent fluctuations in boiling heat transfer and will be represented by error bars for the standard deviation of calculated values of CHF and BHF. Additionally, as a result of nanofluid

boiling, inherent small variation of the amount of deposition along the wire causes deviation in heat flux values.

Nanofluid Characterization

The nanoparticles obtained are Alfa Aesar® colloidal dispersion of silicon(IV) oxide at 15wt/wt% concentration in pure water with 0.83% sodium oxide concentration for stabilization. The initial average particle size is 10nm. The original solution was diluted to various volume percentage concentrations throughout the present work. Sample calculations of the method employed to determine final volume concentrations are presented in Appendix A. Surface tension was measured using calibrated SITA DynoTester® bubble pressure tensiometer. The uncertainty in the measurements are attributed to instrument errors in accuracy and repeatability and are calcluated to be ±1mN/m. The nanofluid pH was measured with a calibrated pH Acorn® 5 Series meter with total instrument error contained within ±0.01 pH. Good mixing and dispersion of the nanoparticles were achieved by 30 minutes magnetic stirring followed by 30 minutes ultrasonic processing (Cole-Parmer®) of each sample. Viscosity measurements were taken with a Brookfield rotational viscometer after mixing and sonicating.

Scanning Electron Microscopy and Energy Dispersive X-ray Spectroscopy Analyses

Surface morphology studies were implemented using SEM and EDS. SEM images were obtained with a Hitachi S3500N Scanning Electron Microscope in two different capture modes – secondary electron (SE) and backscatter electron (BSE) modes. In backscatter electron capture

mode, the material with higher density, i.e., nichrome metal, creates more backscatter of electrons which causes the produced image to look brighter or whiter. Additionally, non-conducting materials (silica) can accumulate charge as a result of image capture, and in secondary electron capture mode, this appears as white spots on the material [33]. To reduce the charging of the material, some of the samples were sputter coated with gold Au and palladium Pd, which are conductive materials.

Investigation of the elemental composition of the silica-deposited nichrome ribbons was performed via energy dispersive spectroscopy (EDS) on a Zeiss Ultra-55 SEM. The instrument produces a primary electron beam (in the present work, 20kV accelerating voltage) which is incident on the sample [33]. This beam causes the ejection of an inner shell electron from the sample, and a higher-energy, outer shell electron then fills the vacancy, giving off an x-ray, whose energy is related to the difference in energies of the respective shells. The EDS x-ray detector senses the intensity of x-rays emitted from the sample by measuring and sorting voltage pulse heights (mV) created by the x-ray and converting them to x-ray energy in keV. Spectra of x-ray counts versus energy then determine the presence of individual elements. Atom and weight percentages of individual elements are also measured by the EDS detector with respect to the total amount of elements measured for the acquisition area size.

CHAPTER FOUR: RESULTS AND DISCUSSION

Effect of Heater Geometry on CHF in Deionized Water

Figure 7 graphically shows the results of CHF and BHF for different size wires and ribbons for pool boiling experiments in DI water. Four runs are shown for each size wire/ribbon. It can be noted that the CHF's of each of the cylindrical wires are clearly higher than that of all the ribbons. Specifically, for a wire and ribbon of similar surface area, the wire has a 25% higher average CHF over the ribbon. This result suggests a possible dependency of CHF on cross-sectional shape. The results show a general decreasing trend of the average CHF with increasing convective surface area. In addition, BHF data are also depicted on the graph, and the plot exhibits a wider-spanning decreasing trend with increasing surface area. Considering the smallest and largest ribbons used, for an 80% reduction in surface area, the data shows a 28% increase in average CHF and an 86% increase in average BHF. It is noticeable that the BHF data cover a wider heat flux range from smallest to largest area compared to the CHF data. This can be attributed to the varied glowing lengths which will be discussed next. Additionally, the scatter in CHF data is due to the uncertainty of the CHF condition, and also stems from the temperature-resistance calibration curve (Figure 6), which has a discontinuity where there is a large temperature jump. The resistance measurement is very sensitive, and it can magnify the uncertainty of the onset of critical condition. The trends are in agreement with the established correlations and data of q_{max} dependence on characteristic length for small heaters [13], [14]. Refer to Appendix B for CHF correlation comparison with that found in literature for ribbons.

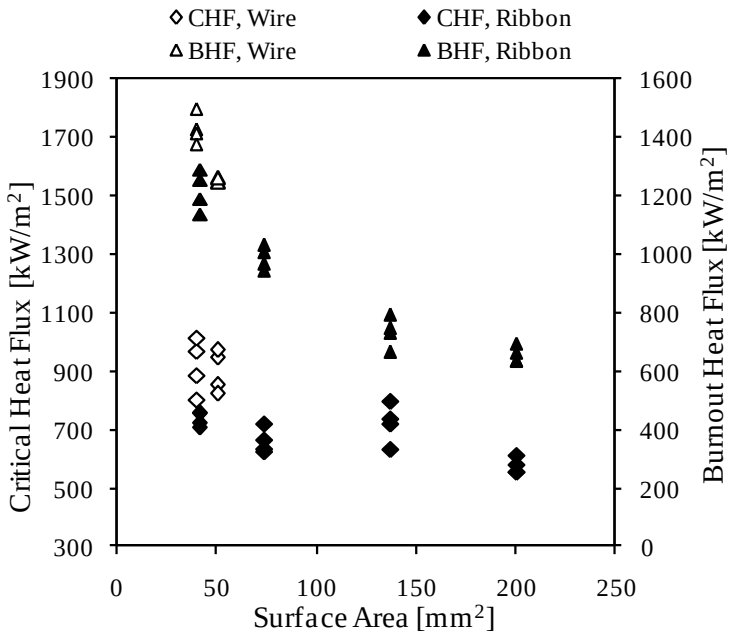

Figure 7: CHF and BHF dependency on heater size and geometry: Experiments in DI water.

Figure 8 shows boiling curve comparisons for representative runs for each wire and ribbon size tested. The decreasing trends of CHF and BHF for increasing ribbon size are noticeable in the graph. Another feature that can be noted is the length of the boiling curve after the CHF point. The length decreases as the surface area of the heater increases. Concurrently, it was observed that the amount in length of wire that glowed after the onset of the critical condition and the duration of the glowing both decreased as the size of the wire was increased. It can be concluded from this observation that the greater the mass of the heater, the more localized heating plays a factor, making it more difficult for heat to spread evenly throughout the entire material. Additionally, this explains the varied difference between CHF and BHF data in Figure 7; the larger difference for small surface area is due to the longer glowing duration which separates the two conditions. As the surface area increases, localized heating causes hot spots, and the CHF

and BHF conditions occur closer together and can even happen simultaneously. Figure 8 also shows that the superheats for CHF for all the sizes lie within approximately 20°C – 35°C, although there is no clear trend for the varied sizes. The CHF wall temperatures corresponding to these superheats were verified with heat transfer correlations presented in the literature and were found to be satisfactorily accurate. See Appendix C for sample verification calculations.

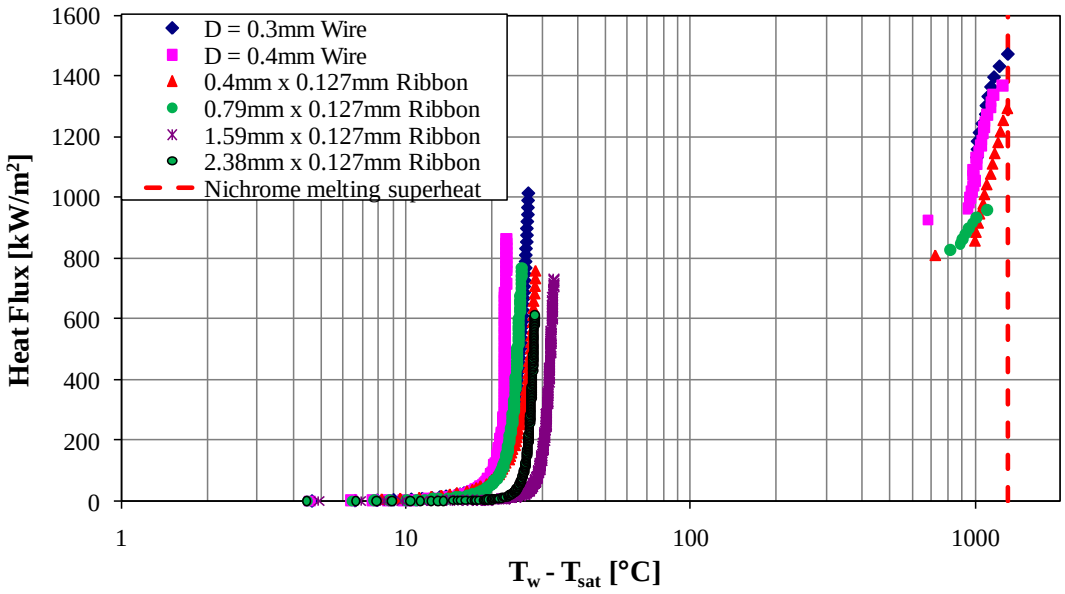

Figure 8: Boiling curve comparison for various sizes of nichrome wires and ribbons in DI water pool boiling.

Effect of Nanoparticle Concentration on pH, Viscosity, and Surface Tension

Properties of the nanofluid were measured to gain an understanding of possible influences on the heat transfer behavior of various nanoparticle concentration. Surface tension results are shown in Figure 9 for various particle concentration. The measurements only slightly deviate and are within the uncertainty limits of ±0.01 (ratio); therefore, this suggests that there is a minimal change in surface tension due to the presence of nanoparticles and should have a negligible effect

on the heat transfer behavior. Measurements taken after the experiment at room temperature show minimal deviation from DI water as well.

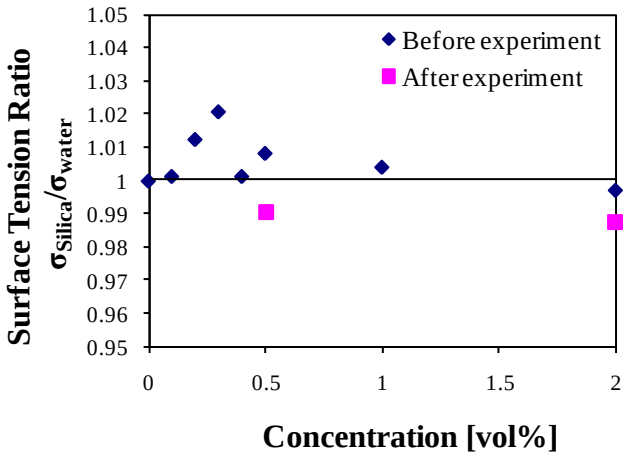

Figure 9: Surface tension of 10nm silica nanofluid at room temperature

Silica nanofluid with water base is a lyophilic dispersion, which signifies that it acquires stability by hydration of the wetting silica surface [31]. The stability of the nanofluid is an important aspect to consider in regards to the agglomeration and settling of the particles. In order to be stable, nanofluid should be far from its isoelectric point – the pH at which the number of positive and negative particles are equal (unstable nanofluid) [11]. The isoelectric point for silica nanofluid is ~3, and the pH was found to be between 9 and 11 for all concentrations used in this study. Figure 10 shows the pH measurements versus particle concentration, and these results confirm the high negative charge of the silica particles as well as the stability of the nanofluid. Experimental observations suggest no agglomeration or settlement before or after the experiment, and the pH before and after the experiment are very similar, with pH after experiment being slightly smaller due to subtraction of particles which deposited on the wire.

Silica particles are highly negatively charged, and high pH indicates a large presence of OH^- ions (hydroxide).

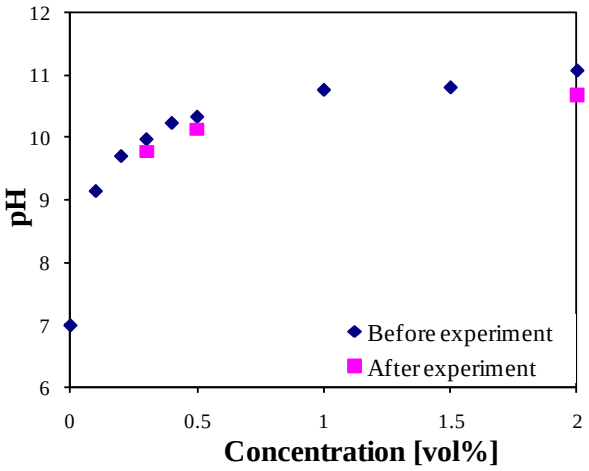

Figure 10: pH of 10nm silica nanofluid at room temperature.

In another study [34], it has been shown that with minimal or no nanoparticle deposition on the wire, there was a 50% CHF enhancement which can be attributed solely to the nanoparticle suspension. Silica nanofluid is intrinsically a lyophilic dispersion, and it is thought to be more wettable than pure water due to the hydration layer of the silica particle. The adsorption of water molecules by the silica particle causes the formation of the hydration layer around the particle. The high pH indicates a high concentration of hydroxyl ions and a high charge density (large particle-particle repulsion) [35]. In addition, it indicates a relatively high amount of hydration of the aqueous silica by way of silanol groups rising from the silica surface. Wen [36] states that nanofluids could exhibit improved spreading and wetting capability in the microlayers underneath growing bubbles causing higher microlayer evaporation. This is inferred from the long-range (a few nanoparticle diameters), structural disjoining pressure theory [37], which postulates that the structural ordering of nanoparticles in very small spaces, i.e., microlayers,

creates an oscillatory excess pressure in the thin film which enhances spreadability of the nanofluid on a surface. Figure 10 displays a significant increase in pH (~9) for a relatively small volume fraction of silica particles (0.1vol%). Thus, it is surmised that the enhanced wettability of the working nanofluid due to the hydration layer (high pH) and structural ordering of particles in the microlayer (enhanced spreadability/wettability) have a combined effect of delaying the dryout of the surface and hence increasing the CHF.

Viscosity measurements, taken after mixing and sonication, are shown in Figure 11 and depict a significant increase in viscosity for higher concentrations of nanoparticle, up to ~40% increase of DI water for 2vol% concentration. At lower concentrations of up to 0.5vol%, the increase in viscosity is less than 15%. Viscosity at higher concentrations rise much more and may affect further enhancement of CHF as we will see later.

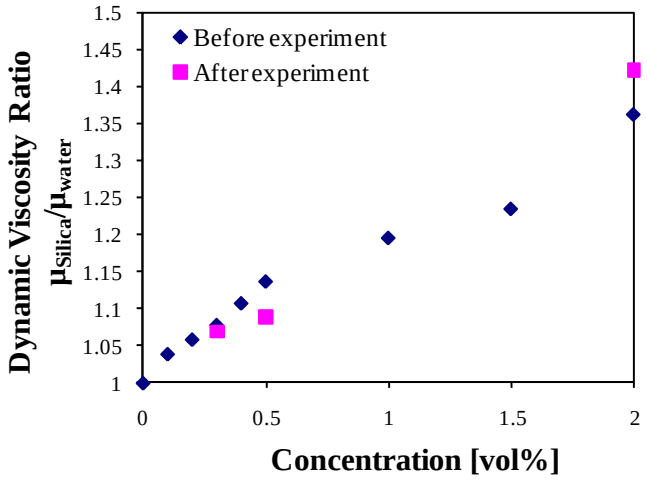

Figure 11: Dynamic viscosity of 10nm silica nanofluid at room temperature.

Because of the deposition, there was a subtraction of particles from the bulk nanofluid after an experiment. Verification calculations were done to determine the mass percentage of the

particles in the nanofluid that was deposited on the heater for an experiment performed to burnout. It was determined that less than 1% of the nanoparticles in the fluid were deposited onto the heater in the worst case scenario (thickest deposition). See Appendix D for calculations.

Effect of Nanoparticle on Thermal Transport

A notable observation in this study was the deposition of nanoparticles on the boiling surface for all concentrations. One study suggests that this porous deposited layer is formed by ionic attraction forces between the negatively-charged silica particles and the electricity generated through the metal ribbon [31]. In addition, the hydrodynamics of the boiling process could also contribute to the formation of the deposition. It is postulated that microlayer evaporation with subsequent settlement of the nanoparticles contained in it could be the mechanism which forms the porous layer [11].

Flow visualization

The flow visualization in Figure 12 shows a comparison of 3 different nanoparticle concentrations and also pure DI water (columns) for pool boiling done with 0.79mm x 0.127mm ribbon. (See Appendix E for flow sequences for all concentrations.) For each concentration, a progression of heat fluxes (rows) are shown, with the last picture in each sequence representing the moment just before burnout. A comparison of these picture frames shows that while the ribbon in water burns out around 1000kW/m^2, the ribbons in the nanofluid have an extended life. Features that are noticeable in the early nucleate boiling regime for increasing concentration are

the presence of small bubbles and an increased bubble number density. This result can be attributed to the increased porosity and higher nucleation site density of the deposition layer as concentration is increased, rendering a smaller bubble departure radius. It was shown in another study [17] that a direct result of the porous layer was higher nucleation site density. There is evidence in the flow visualization that external vaporization and microconvection due to increased active nucleation sites are the cause for enhancement, as noted by [17].

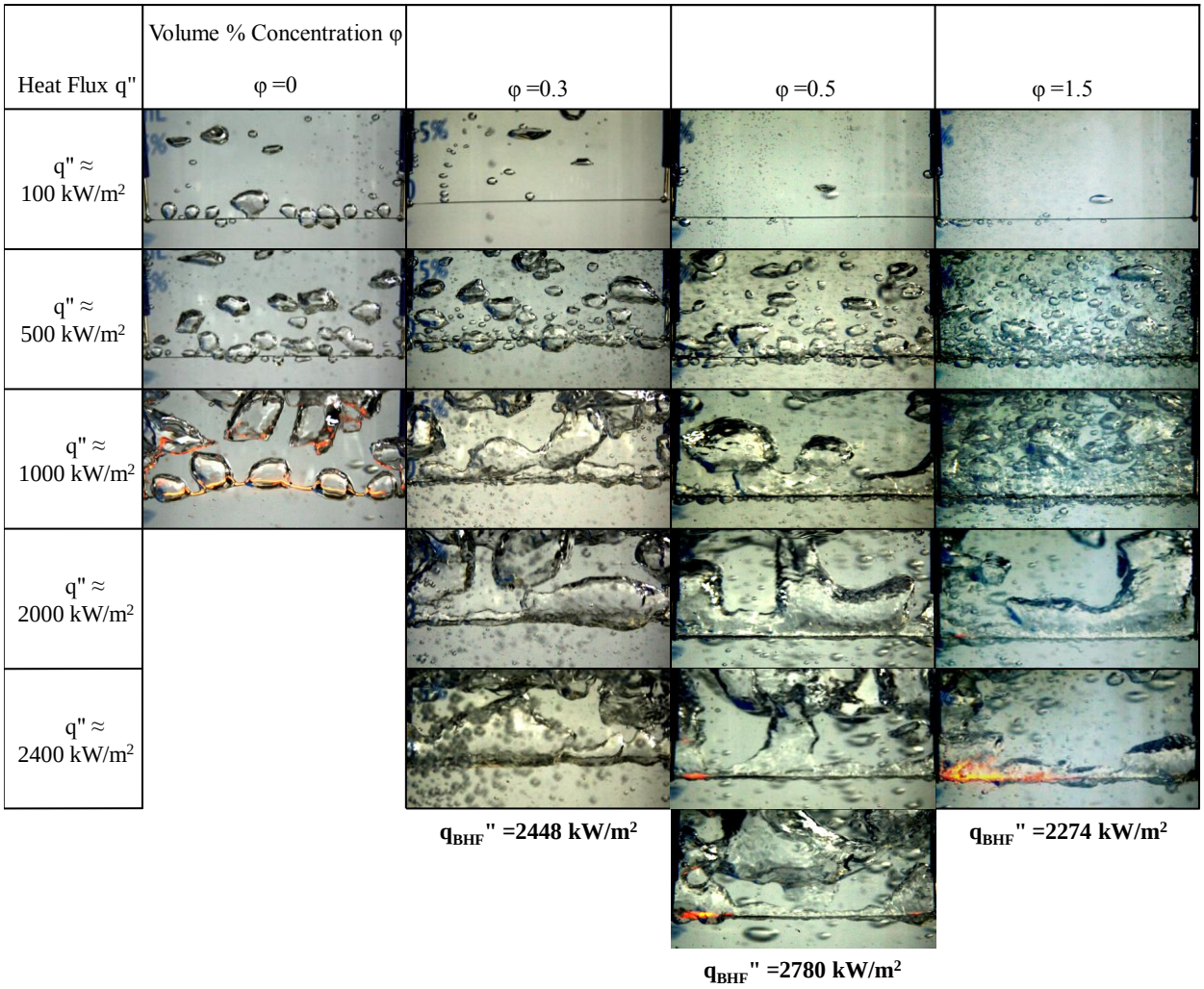

Figure 12: Flow visualization of the pool boiling phenomenon: Particle concentration comparison at various heat fluxes.

Another feature that is apparent in the flow visualization in Figure 12 is the amount of glowing present, or the glowing length, which can be seen in the bottom picture in each column. For pure DI water, the entire ribbon glows after reaching CHF and subsequently breaks. For relatively small concentration of nanofluid, the glowing length is small (only a few millimeters), while it is longer for higher concentrations. The hydrodynamic implication of this is that for small particle concentration (thin porous layer), the moment there is a local dryout of the surface, the temperature increases suddenly under the imposed high heat flux. In this case, the ribbon immediately burns out at that local hot spot, as contrasted by the gradual local to global dryout for higher concentrations (~1.5vol%), as evidenced by the longer glowing length. The sudden burnout can be explained by the hot/dry spot theory proposed by Theofanous et al. [4]. DNB occurs when the evaporation recoil force overcomes the surface tension force which acts to rewet the surface. A dry spot that has developed at high heat flux can be reversed by subsequent rewetting. The increased wettability of the nanoparticle-coated surface causes a delay in the onset of CHF condition, and when it does occur there is a quick burnout of the ribbon. Whereas, for higher concentrations, adverse effects in heat transfer from the heater surface (discussed later) are manifested in the longer glowing length of the ribbon.

There is clearly an overall CHF enhancement for all concentrations measured. In the high heat flux region (slugs and columns regime), it can be seen that the vapor bubbles are relatively large and non-uniformly shaped (Figure 12). These vapor bubbles behave like those of the mushroom vapor bubble theory [5], with feeder jets supplying large amounts of vapor to the mushroom bubble and hence extending heat flux range of the heater. As indicated by [11], the porous

surface is more wettable compared to clean surfaces, so this can additionally enhance the cooling effect in the high heat flux range.

CHF Enhancement for Various Size Wires and Ribbons

Nanosilica pool boiling experiments were done with various wires and ribbons at several particle concentrations, and the results for CHF and BHF percentage increase over DI water are shown in Figure 13 with each point representing one run. It can be seen that the 0.4mm ribbon in 0.3vol% silica exhibited up to 340% CHF enhancement and approximately 175% BHF enhancement. The 0.32mm diameter wire showed a CHF enhancement of 285% over pure water for a nanosilica concentration of 0.2vol%. Additionally, Figure 13 shows that CHF and BHF display a non-monotonic behavior with respect to concentration for all cylindrical wires and ribbons. A detailed analysis and discussion regarding the non-monotonic behavior of CHF and BHF as a function of concentration will be presented later with data collected from 0.79mm ribbon experiments.

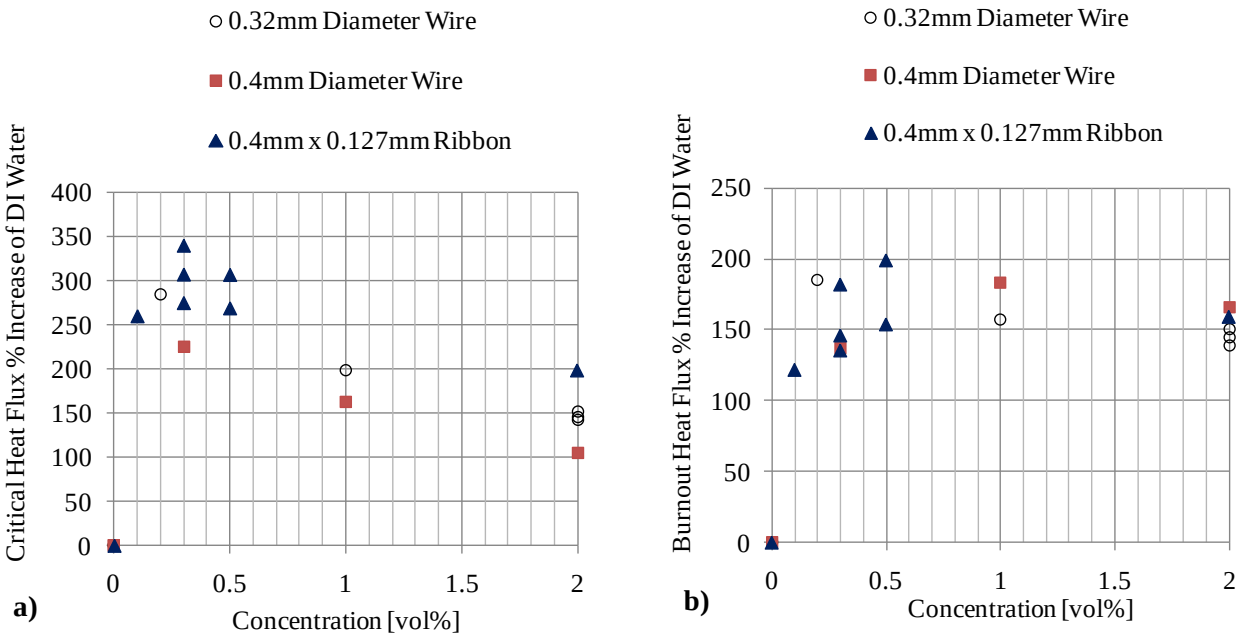

Figure 13: a) CHF and b) BHF percentage increase over DI water for various concentration 10nm silica pool boiling of wires and ribbon.

As shown in Figure 14 and Figure 15 for 1.59mm and 2.38mm ribbons, respectively, CHF was attained in DI water pool boiling but due to equipment limitations the experiments with nanosilica could not be completed to burnout or CHF. However, given the results from the smaller heaters, it can be inferred that some amount of CHF enhancement can be expected for these ribbons as well.

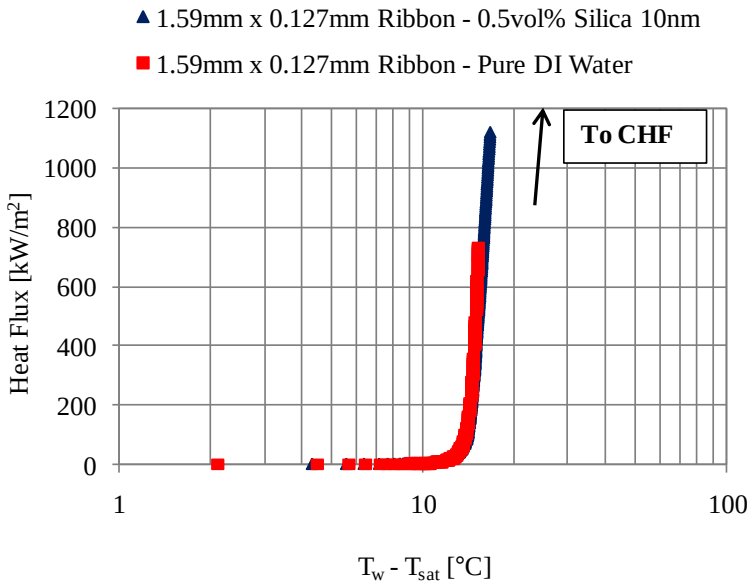

Figure 14: Partial boiling curve for 1.59mm Ribbon in 0.5vol% silica and DI water.

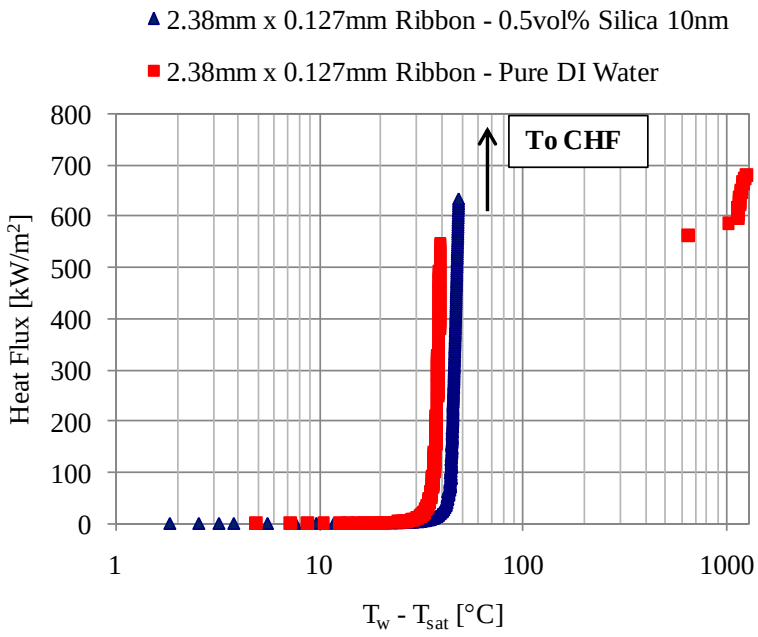

Figure 15: Partial boiling curve for 2.38mm ribbon in 0.5vol% silica and DI water.

In pool boiling experiments using 0.79mm x 0.127mm ribbons, a 250% to 300% enhancement in CHF has been found for silica nanoparticle concentrations less than 0.5vol% (Figure 16a). As Figure 16a shows, the CHF versus particle concentration curve exhibits a non-monotonic behavior, with maximum CHF enhancement occuring between 0.2vol% and 0.4vol%. As concentration is increased further, the CHF decreases and apparently settles to a nominal value. A similar behavior is also seen for BHF versus concentration (Figure 16b); maximum BHF enhancement of ~180% is observed between concentrations 0.2vol% to 0.4vol% and subsequently decreases with further increase of concentration.

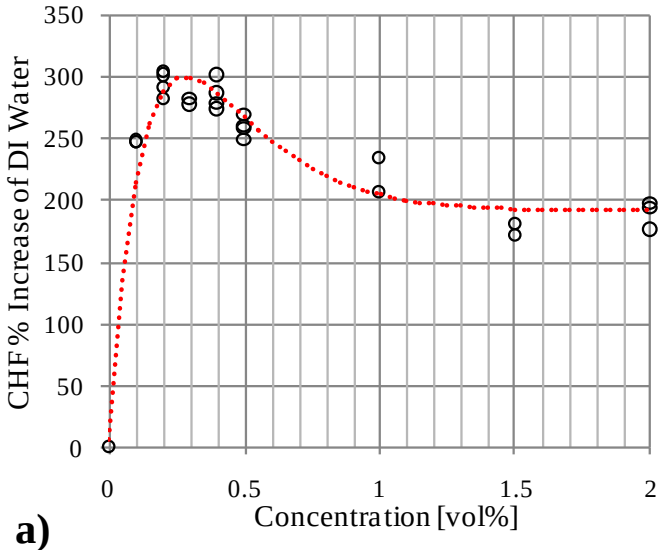

a)

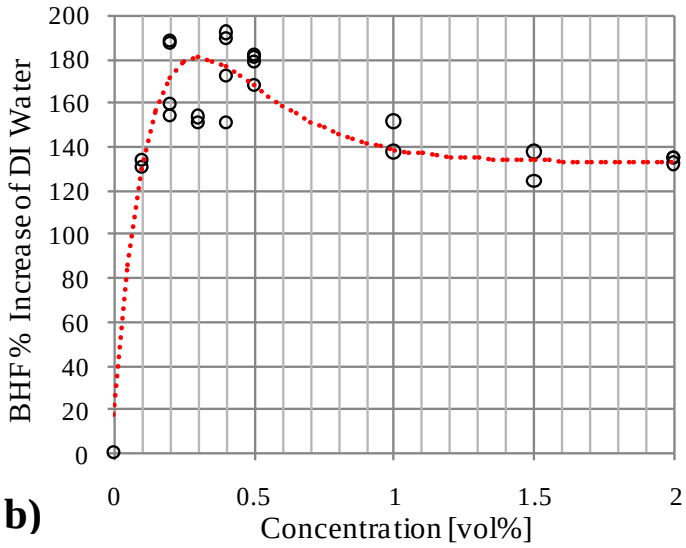

Figure 16: a) CHF and b) BHF percentage increase over DI water versus concentration of 10nm silica, 0.79mm x 0.127mm ribbon.

A concurrent event is found in Figure 17, where representative pool boiling curves for each concentration show an increasing wall superheat at CHF as concentration increases. The increasing wall superheat at CHF is highlighted in Figure 17b with the representative pool boiling curves graphed on a linear plot up to CHF. An investigation of why the superheat at CHF increases in the high heat flux range will illuminate several mechanisms that influence the heat transfer behavior of nanofluids.

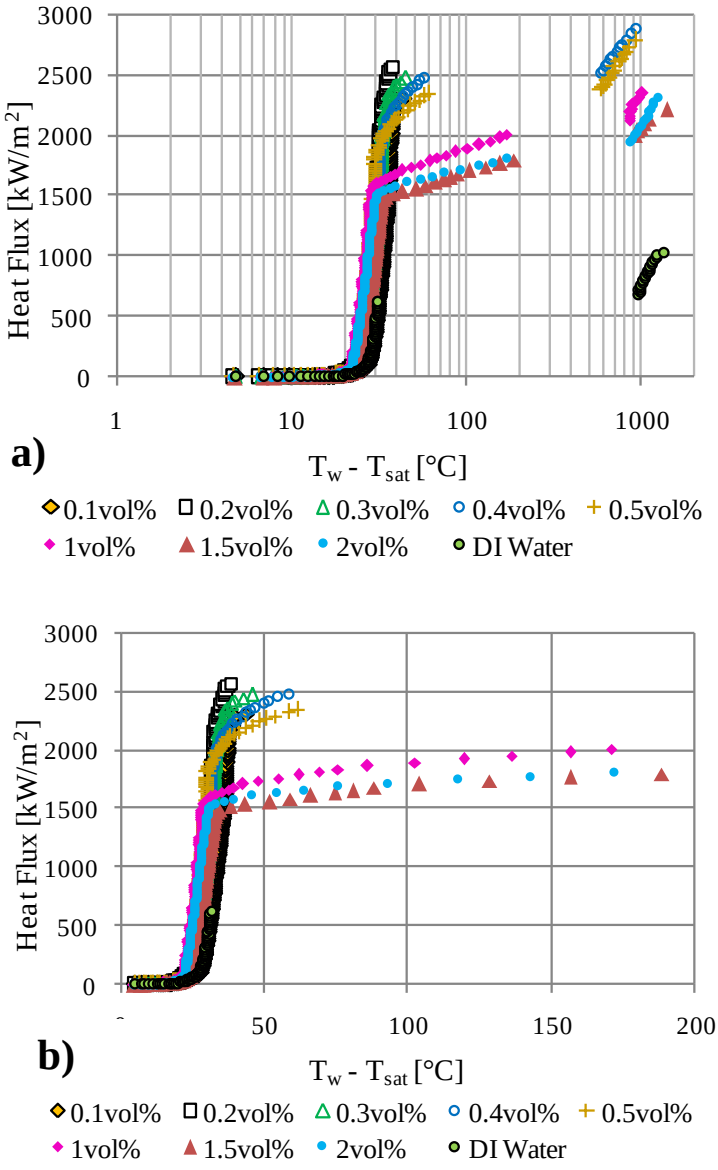

Figure 17: Pool boiling curves for different concentration 10nm silica, 0.79mm x 0.127mm ribbon, a) semilog plot, b) linear plot.

The general increasing trend of deposition height at CHF with increasing particle concentration can be seen in Figure 18a. Error bars represent the standard deviation of deposition height for one individual ribbon and the standard deviation of the CHF resistance ratio for 2-4 runs. The experimental results suggest that the increasing thickness of the porous layer increases the

electrical resistance of the circuit, the dependency of which is depicted in Figure 18a, which shows that for concentrations less than 0.5vol%, the resistance and deposition increase quickly and then more gradually after 0.5vol%. In Figure 18b the general increasing trend of wall superheat at CHF with particle concentration can be seen, as well as the resistance ratio from which the temperature was calculated via the resistance-temperature correlation. It can be seen that for relatively small concentration (~0.1vol%), the wall superheat at the critical heat flux condition has not changed significantly with respect to pool boiling in pure water. However, the CHF wall superheat continues to increase rapidly to 0.5vol% and more gradually after 0.5vol%, possibly suggesting that the nucleation site density at high heat flux levels starts increasing beyond 0.5vol%, signifying a more porous layer for higher concentrations. The electrical resistivity of silica is $>10^{12}$ Ωm, which is significantly larger than that of nichrome ($\rho = 1.08*10^{-6}$ Ωm); therefore, it is gathered from figures a) and b) that when the deposition thickness increases, the resistance increases, which inherently increases the superheat. The increasing superheat along with the decreasing heat transfer from the heater surface (decreasing CHF) cause the metal to retain more heat, raising its temperature significantly more compared with lower concentrations. Physical evidence of the wall superheat increase at CHF with increasing particle concentration is observed in the present study as increasing glowing length at CHF for increasing concentrations (Figure 12). Therefore, it appears that the competing mechanism for CHF/BHF as concentration increases is enhanced wettability versus a thermal insulation coating effect. It is further commented that although the relative porosity is thought to increase after 0.5vol%, this does not outweigh the detrimental effects of the thermal insulation effect.

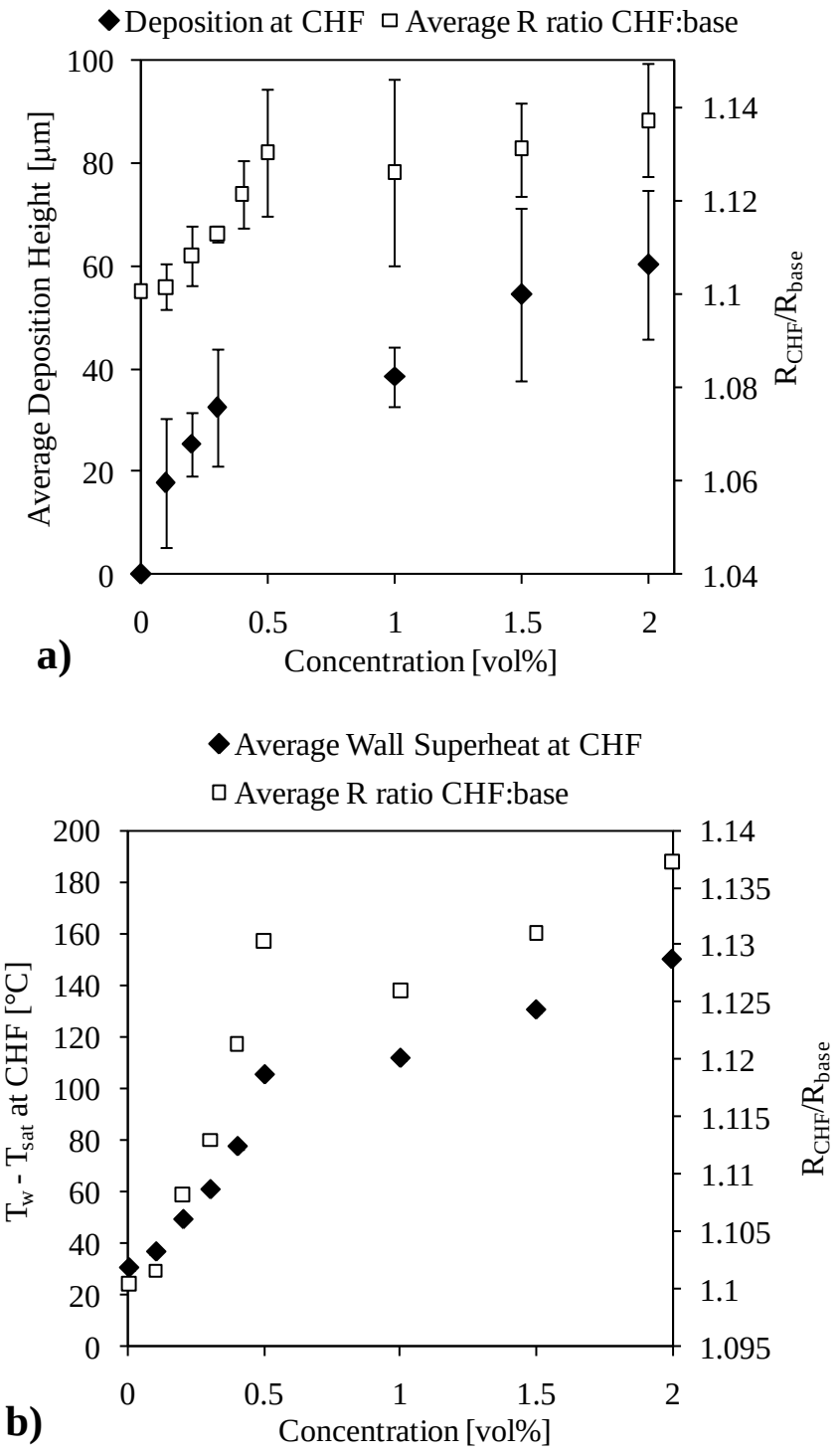

Figure 18: Resistance ratio at CHF, and a) Average silica deposition height at CHF, and b) Wall superheat at CHF versus particle concentration.

It was shown in the flow visualization that the glowing length of the nichrome ribbon increases as the concentration increases. Glowing length measurements were taken by careful inspection of the flow visualization pictures of the moment just before burnout of the ribbon, and Figure 19 shows a graphical interpretation of this occurrence. The figure shows that in DI water, the entire length of the considered portion of the ribbon between the voltage sense wires glows. For small concentration 0.1vol% nanosilica, only a small local portion of the entire ribbon glows. Furthermore, as the nanoparticle concentration is increased, the amount of ribbon length that glows increases as well. It is thought that the increased glowing of the ribbon for larger particle concentrations is an indicator of the increased thermal insulation effect that is caused by the thicker deposition of relatively high concentrations of silica. A discussion of the hydrodynamic implications of the thermal insulation coating follows.

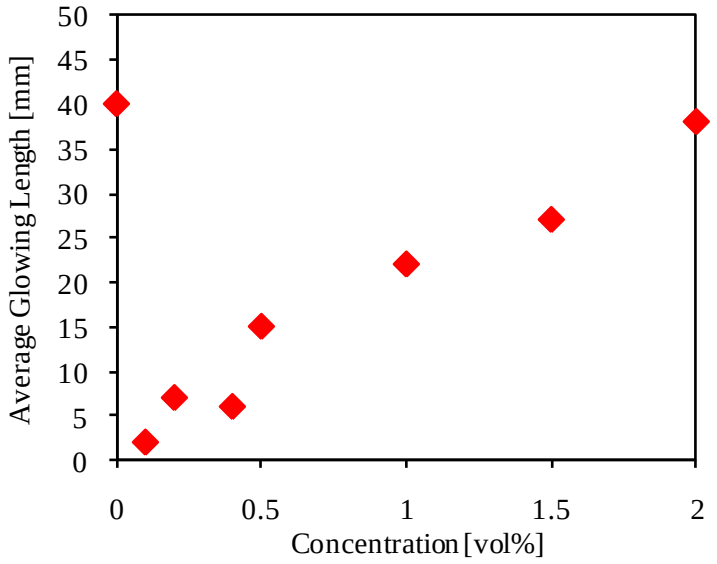

Figure 19: Average longitudinal glowing length of ribbon versus particle concentration.

It may be conjectured that because of the thicker layer on the ribbon, less amount of liquid can reach the sublayers and ultimately the metal surface. Surface characterization experiments done

by Kim et al. [24] showed that the type of working fluid also has an effect on capillary wicking in addition to the surface coating itself. They postulate that boiling of nanofluid on a nanoparticle-coated surface could in fact cause clogging of micro-flow-passes due to the suspended nanoparticles. It can be inferred that as particle concentration of the nanofluid increases, the effect of capillary wicking diminishes since there are increasing amounts of suspended particles in the nanofluid. Alternatively, it has been suggested that the CHF reaches a plateau for certain critical value of coating thickness [38]. Thome [39] notes that the coating thickness should be maintained thinner than a stipulated value in order to avoid an additional thermal resistance by the particles and entrapped vapor, effects of which have been shown in this work. Additionally, in other work it has been seen that as particle concentration increases, the contact angle gradually increases, effectively reducing the enhancement of wettability [11]. With the preceding analysis, it may be concluded that the combined effect of increasing contact angle, reduced effect of capillary wicking, increasing viscosity, and increasing thermal resistance contributes to the effective decrease of CHF as particle concentration increases (the roll-over in Figure 16).

Effect of Heat Flux on Deposition

Repeated experiments were done in which the current through the heater was continually increased up to a certain predetermined value and was subsequently stopped. Silica deposition was measured with calipers to find the deposition height above the metal surface for intermediate heat fluxes before the CHF condition in order to investigate what kind of trend there exists related to the growth of deposition versus heat flux increase. Figure 20 shows the pool boiling

curves for each case analyzed with SEM and energy dispersive spectroscopy (EDS), the last point signifying where the experiment was stopped. Cases 1 – 3 pertain to 0.2vol% silica for increasing heat fluxes, and cases 4 – 6 pertain to 2vol% silica for increasing heat fluxes.

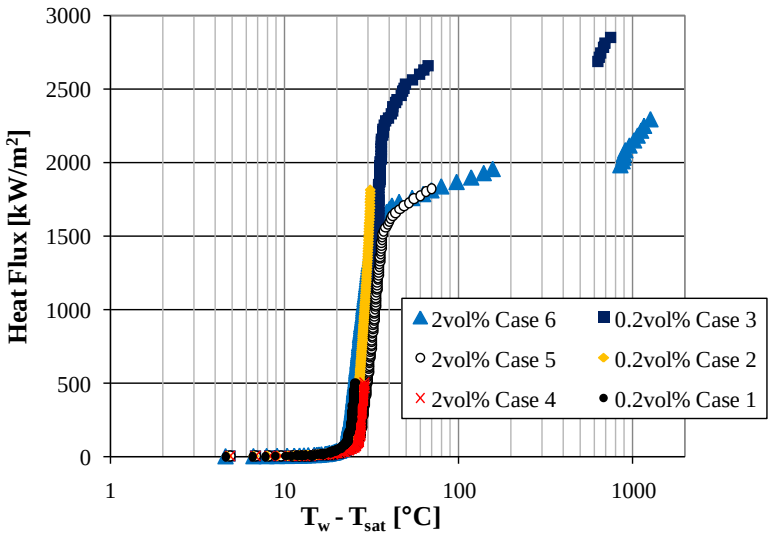

Figure 20: Pool boiling curves of experimental runs used for SEM/EDS analysis 0.2vol% and 2vol% silica on 0.79mm x 0.127mm ribbon.

Figure 21a depicts the average deposition height versus the heat flux when each experiment was stopped. Each point represents one run, and the error bars signify the standard deviation of the variation of deposition height on each individual ribbon. The trend appears to be nonlinear in nature, in which the deposition increases by a factor of 1.6 in a heat flux span of 1300 kW/m^2, and then increases by a factor of 3 in a heat flux increase of around 1000 kW/m^2. Note that the latter increase occurs between ~2000 to 3000 kW/m^2, a relatively high heat flux. The CHF dotted line indicates where the CHF occurred before the graphed BHF data point. Due to the fact that the jump in temperature (glowing) in the 0.2vol% case for the run depicted as BHF was very brief in time and covered only a small portion of the wire, it is accurately presumable that the

deposition amounts for CHF and BHF for this run in particular were very close. This insinuates that no conclusions can be drawn with regard to the differences between CHF and BHF in the low concentrations (< 0.5vol%) since these two conditions happen either simultaneously or just a few seconds apart. Nevertheless, it can be inferred from this graph that a higher rate of deposition can be attributed to high heat fluxes. (In the foregoing analysis, the rate of deposition was verified by plotting deposition versus inputted current which was incremented every 3 seconds. The curves were qualitatively the same.)

A similar trend as in the 0.2vol% case can be seen for experiments with 2vol% silica shown in Figure 21b. The deposition increases two fold in a span of 1300 kW/m^2 of heat flux and increases by a factor of 3 in a span of approximately 500 kW/m^2 (half the heat flux amount in 0.2vol%). A large increase in deposition occurs after and encompasses the CHF point, so it appears as though very high temperatures as well as high heat fluxes additionally accelerate the rate of deposition. For the higher concentrations, the CHF and BHF conditions are more distinct in their occurrences; therefore, differences in features are more noticeable, for example, deposition.

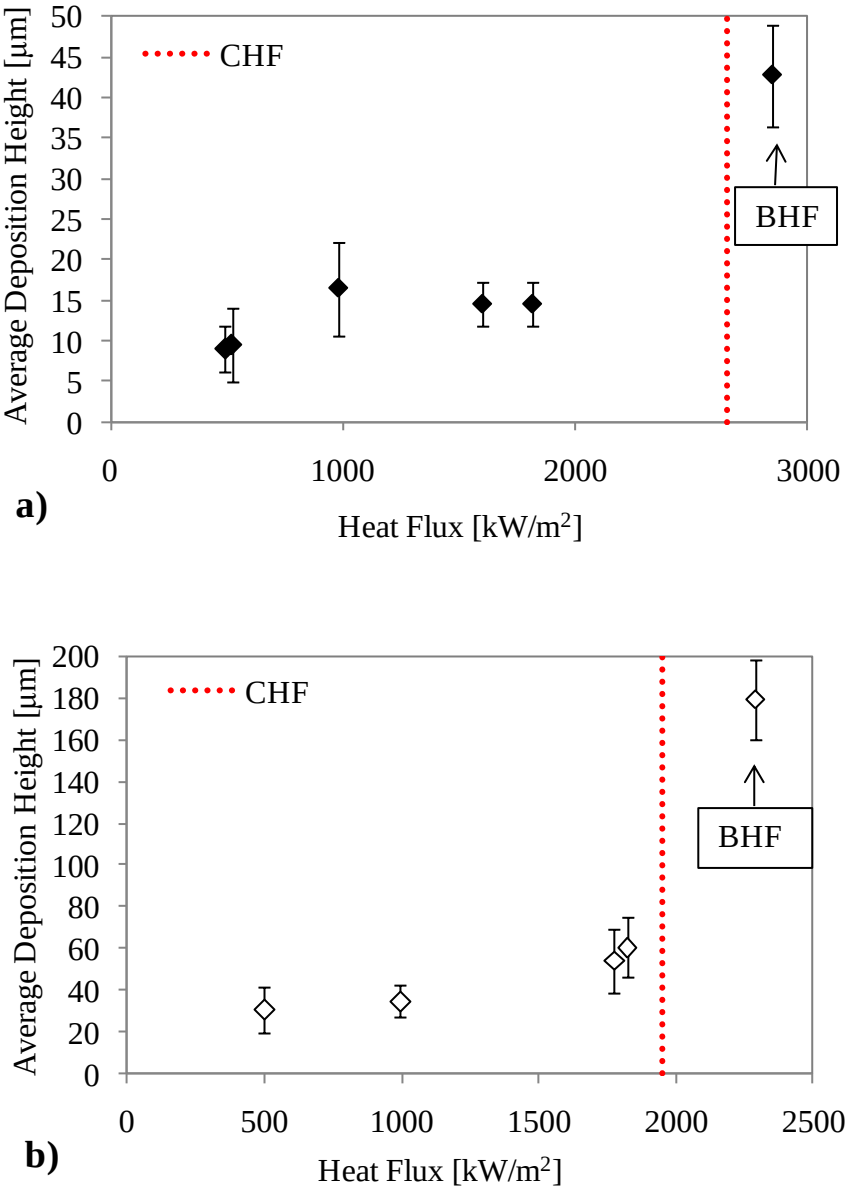

Figure 21: Average deposition height versus heat flux for individual runs, 0.79mm x 0.127mm nichrome ribbons, a) 0.2vol% silica, b) 2vol% silica experiments.

Figure 22 shows the difference between the deposition amounts at CHF and BHF for the range of concentrations tested. The lower concentrations show the CHF and BHF deposition amounts superimposed because these conditions happen simultaneously on average. The higher

concentrations show a large difference between the CHF and BHF deposition heights, suggesting that the relatively higher rate of deposition for larger concentrations is related to the glowing amount, which was shown to be a consequence of the thermal insulation effect. In other words, the thicker coating in higher concentrations causes the metal to retain more heat which is manifested in the glowing amount, and the higher temperatures cause the rate of deposition to increase, which is reflected in the wide gap in CHF and BHF deposition heights.

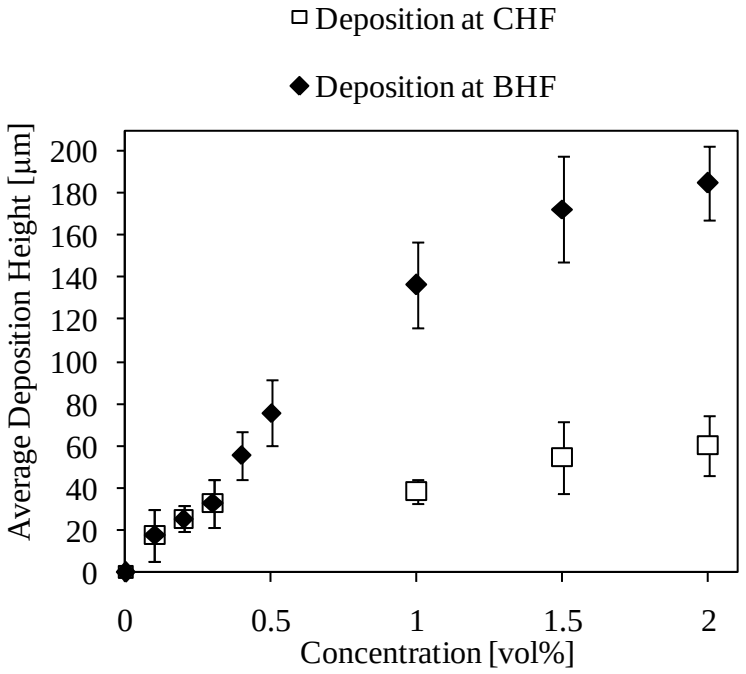

Figure 22: Average deposition heights at CHF and BHF versus particle concentration.

SEM Images and Analysis

Figure 23 shows a schematic of the cross-sectional and top views as a reference for the SEM and EDS analyses that follow in this study. Cross-sectional views were obtained on the Hitachi SEM, and top views were obtained on the Zeiss SEM along with EDS data. Figure 24 and

Figure 25 each show a sequence of SEM images corresponding to increasing deposition heights. Figure 24 shows a) Case 1 = 10μm, b) Case 2 = 14.5μm, and c) Case 3 = 42μm. Figure 25 shows a) Case 4 = 30.5μm, b) Case 5 = 60.3μm, and c) Case 6 = 180μm. The images show that the deposition heights are equal on the top and bottom boiling surfaces, validating the averaged, top-surface heights obtained by caliper measurements. A comparison of the images in the figures reveals that the thinnest deposition has consistent texture, whereas greater thicknesses increasingly show non-uniformities in the form of cracks, voids, and large agglomerates. Figure 24c shows the edge where burnout occurred. The roughness of the protruding nichrome metal indicates oxidation of the metal. This image also reveals that the silica deposition forms as an even coating around the entire perimeter of the ribbon, and there are noticeable agglomerates and voids throughout the deposition. The EDS spectra plot in Figure 24 shows that the general elemental composition of the surface consists of the expected elements: silicon, oxygen, nickel, and chromium. A small amount of carbon was detected due to the carbon adhesive. Figure 25a) and b) show agglomerates of silica on the top, and c) shows significant cracks, which exemplifies the brittleness and porosity of the deposition layer. Also, the numerous cracks may contribute to lower the relative density of thicker layers, implying that as a layer thickens, the average density may decrease as a result of loose packing. As shown in the EDS spectra plot in Figure 25, there was no detection of nickel or chromium, supporting the fact that the electron beam penetrates to a certain depth depending on the thickness and density of the medium. For the thickest deposition at 180μm, the beam could not penetrate to the nichrome ribbon. Further analyses on beam depth regarding relative densities will be discussed later. Sodium was detected due to the small percentage of sodium oxide stabilizer in the original solution. The count levels

of the various elements are a product of quantum mechanics process and do not indicate relative composition between the elements for any given sample, since there is not a linear relationship between counts and relative composition. The atom and weight percentages, explored next, give insight with regard to the element comparison of the samples.

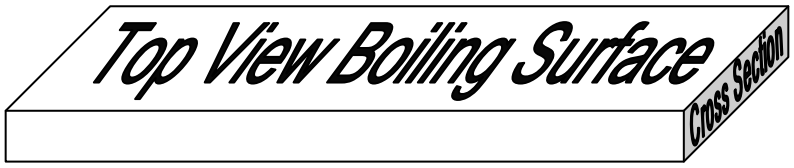

Figure 23: Schematic of view orientation of SEM and EDS analyses.

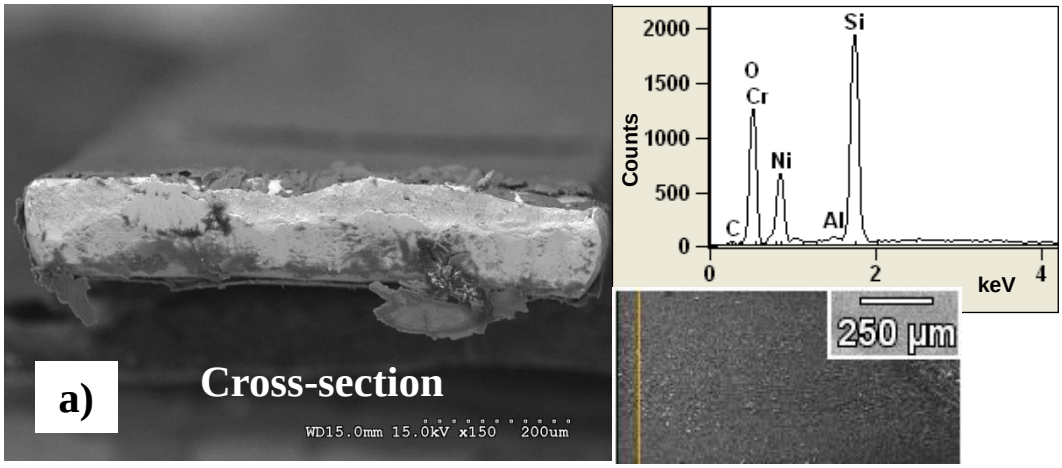

Top View

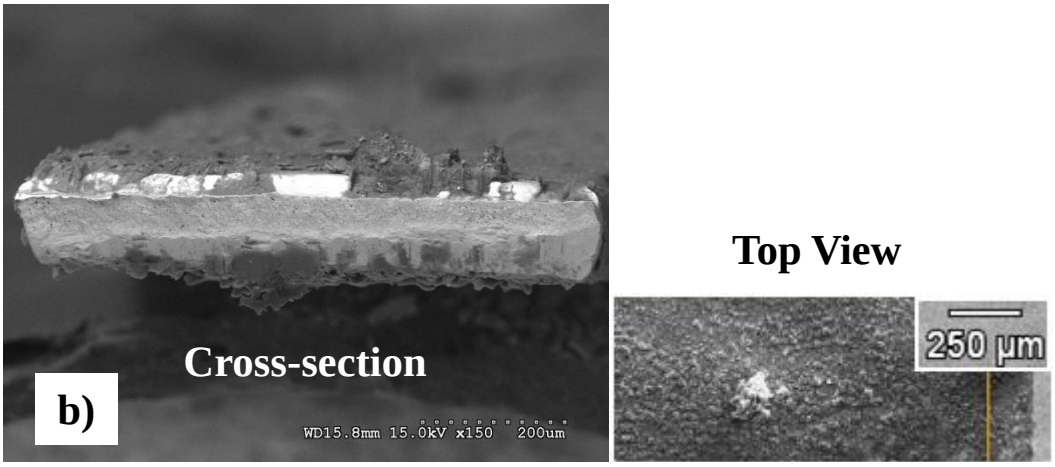

Top View

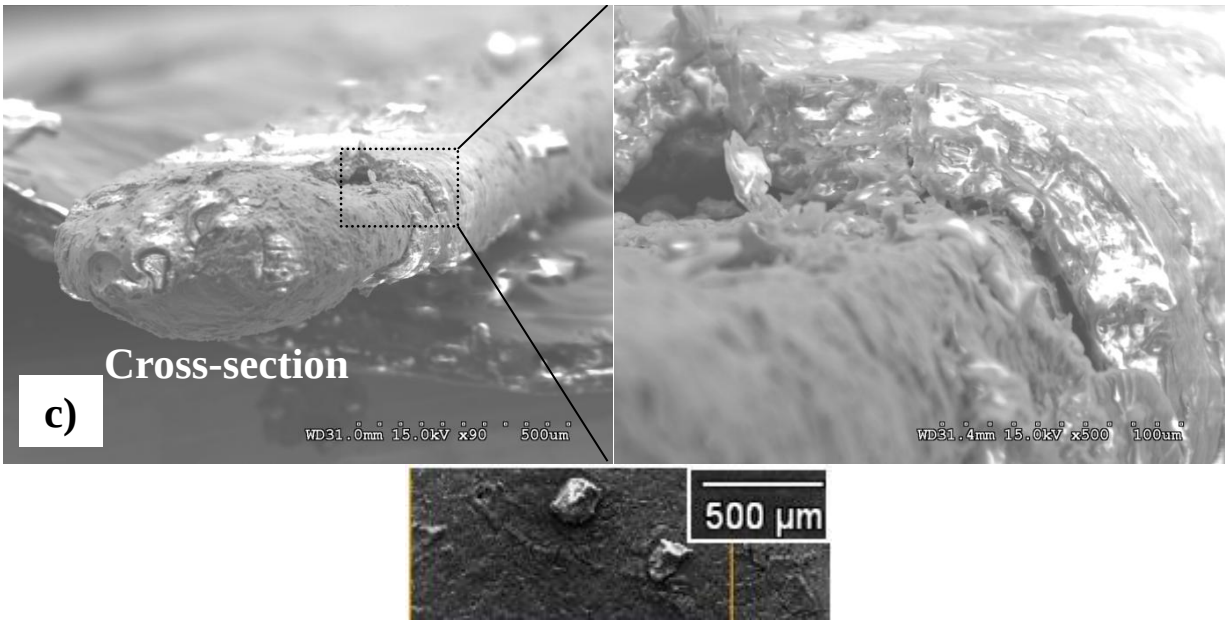

Figure 24: SEM cross-sectional views and top views of 0.2vol% silica deposition on nichrome ribbon, a) 10µm deposition at heat flux 503 kW/m^2 – BSE image, SE image & EDS spectra plot, b) 14.5µm deposition at 1816 kW/m^2 – BSE image, SE image, c) 42µm deposition at burnout heat flux 2847 kW/m^2 – SE images of burnt out edge of ribbon & close up of deposition surrounding burnout region.

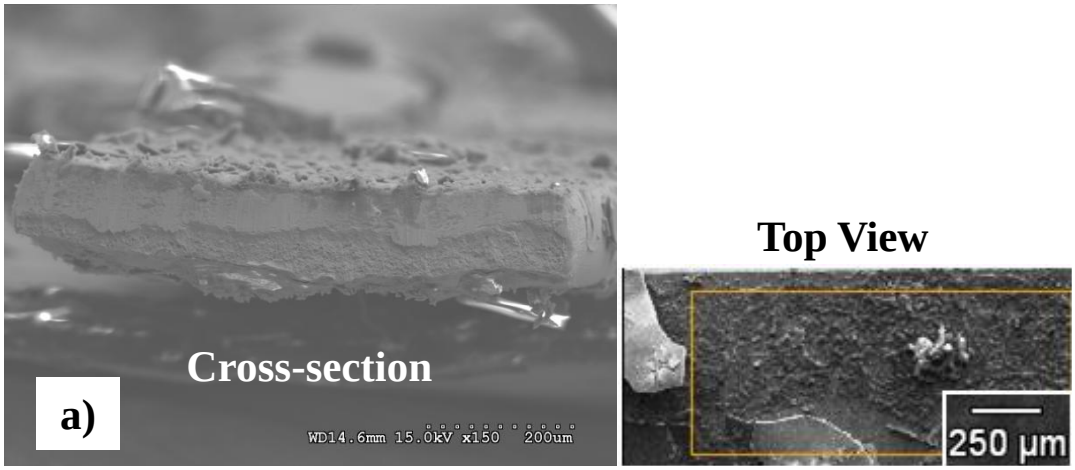

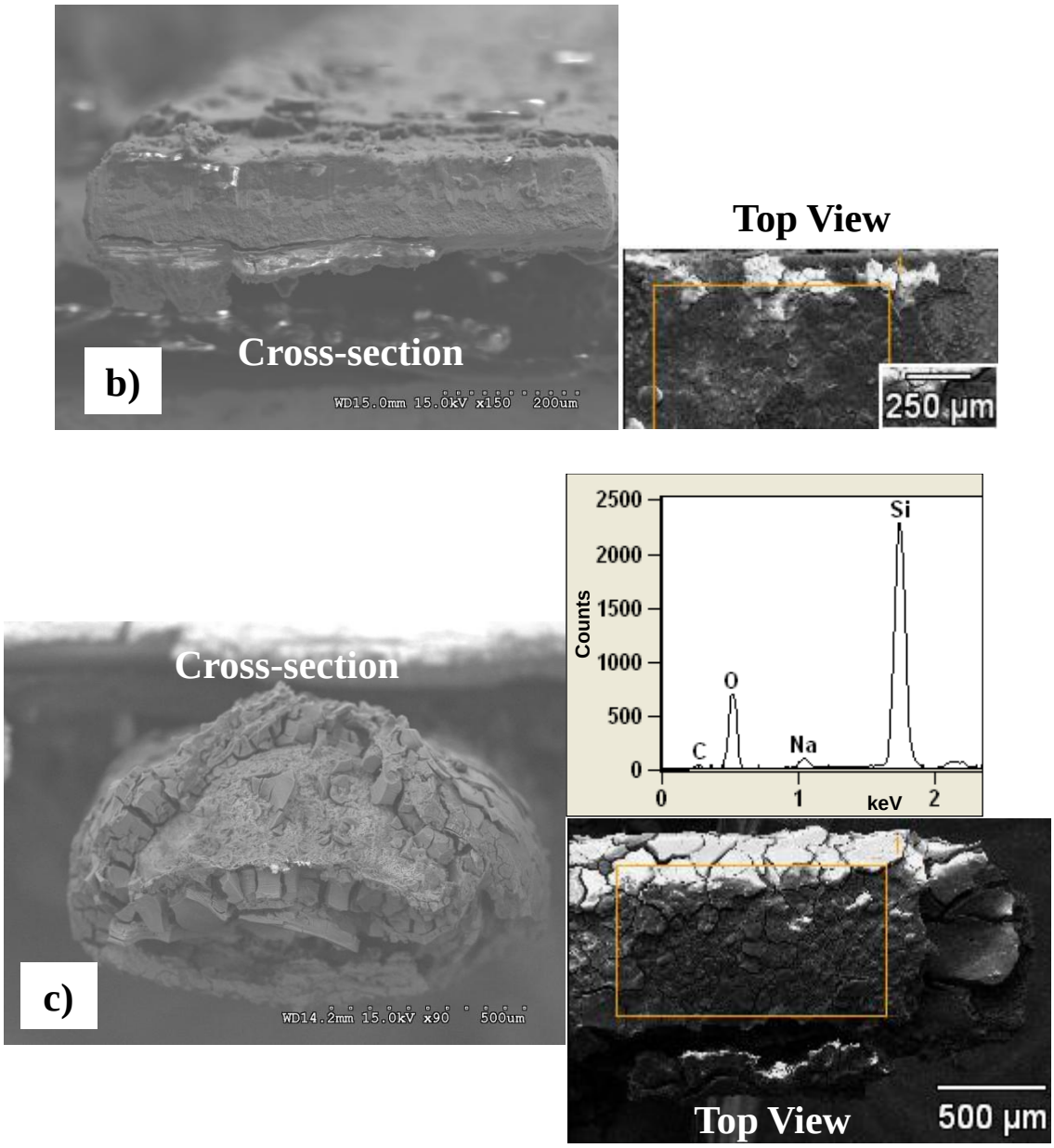

Figure 25: SEM cross-sectional views and top views of 2vol% silica deposition on nichrome ribbon, a) 30.5µm deposition at heat flux 500 kW/m^2 – SE images, b) 60.3µm deposition at 1823 kW/m^2 – SE images, c) (inverted cross-section) 180µm deposition at burnout heat flux 2291 kW/m^2 – BSE image & EDS spectra plot.

Energy Dispersive Spectroscopy Analysis

EDS was done on the top boiling surface for all samples at 20kV accelerating voltage to ensure an equal penetration depth into all the samples, given that the densities are all equal. The lateral acquisition area on the top of the surfaces for cases 1 – 6 are 0.703mm^2, 0.762mm^2, 1.26mm^2, 0.819mm^2, 0.625mm^2, and 0.812mm^2, respectively. Atom and weight percentages measured with an EDS detector give information with respect to relative changes in element amounts from sample to sample. The atom and weight percentages of all the elements detected (rows) are listed in Table 3 for cases 1 – 3 (columns) of 0.2vol% silica and in Table 4 for cases 4 – 6 of 2vol% silica. Inspection of Table 3 shows that as the deposition increases (left to right), the amount of nickel detected decreases because the electron beam has to penetrate increasing amounts of deposition and cannot reach the metal. In case 3 which had deposition height 42μm, no appreciable nickel was measured. In comparison, Table 4 case 5 had more deposition height 60.3μm, and the electron beam penetrated through the entire deposition layer and slightly into the substrate, given that a small amount of nickel was measured (at.% and wt.%). Therefore, the silica deposition of case 5 would seem to be less dense than that of case 3 in order for the electron beam to pass through the thicker layer to the metal substrate. In a similar example, nickel was measured in both cases 2 and 4, signifying that the beam penetrated to the substrate in both cases. Case 4 had double the deposition height compared with case 2 (30.5μm vs. 14.5μm), and case 4 still penetrated through the entire silica layer finally to detect almost the same amount of nickel and chromium as in case 2. Moreover, case 4 showed less silicon (at.% and wt.%) than case 2, possibly implying that the average density of the silica layer in case 4 is less than in case 2. It is deduced by a comparison of both tables that the average density of the silica deposition

layer in the 2vol% silica experiments is less than that in the 0.2vol% cases. The lower density causes the deposition to be more porous and evidence of this can be seen in the flow visualization as the higher bubble number density for higher concentrations (Figure 12).

Table 3: EDS data for increasing deposition/heat flux of 0.2vol% silica on 0.79mm x 0.127mm nichrome ribbons, a) weight %, b) atom %.

0.2vol% Silica			
a) Elements by Weight %	**Deposition at Indicated Heat Flux**		
	10 µm at 503 kW/m^2 Case 1	**14.5 µm at 1816 kW/m^2 Case 2**	**42 µm at 2847 kW/m^2 (BHF) Case 3**
Silicon	19.3	28.56	37.91
Oxygen	14.92	31.16	43.62
Nickel	45.99	25.63	--
Chromium	14.29	7.72	--
Carbon	3.8	5.24	12.07
Sodium	1.47	1.66	--
Aluminum	0.23	0.03	--
Palladium	--	--	2.44
Gold	--	--	3.96
Totals	100	100	100
b) Elements by Atom %			
Silicon	22.41	25.05	26.34
Oxygen	30.41	47.98	53.21
Nickel	25.54	10.75	--
Chromium	8.96	3.66	--
Carbon	10.32	10.74	19.61
Sodium	2.09	1.78	--
Aluminum	0.27	0.04	--
Palladium	--	--	0.45
Gold	--	--	0.39
Totals	100	100	100

Table 4: EDS data for increasing deposition/heat flux of 2vol% silica on 0.79mm x 0.127mm nichrome ribbons, a) weight %, b) atom %.

2vol% Silica			
	Deposition at Indicated Heat Flux		
a) Elements by Weight %	**30.5 µm at 500 kW/m^2 Case 4**	**60.3 µm at 1823 kW/m^2 Case 5**	**180 µm at 2291 kW/m^2 (BHF) Case 6**
Silicon	26.16	43.12	38.16
Oxygen	29.61	41.88	43.31
Nickel	20.46	1.23	--
Chromium	7.1	--	--
Carbon	12.24	7.64	11.64
Sodium	2.27	2.74	3.07
Palladium	2.16	--	3.82
Gold	--	3.39	--
Totals	100	100	100
b) Elements by Atom %			
Silicon	21.14	31.04	26.11
Oxygen	42.01	52.92	52.01
Nickel	7.91	0.42	--
Chromium	3.1	--	--
Carbon	23.13	12.86	18.62
Sodium	2.25	2.42	2.56
Palladium	0.46	--	0.70
Gold	--	0.34	--
Totals	100	100	100

An additional finding from the weight percentage data of EDS is that the nickel to chromium weight percent ratio calculated from Table 3 and Table 4 was found to be between 2.8 and 3.3 wt.% which is lower than the manufacturer specified NiCr 80/20 wt.%. The lower value means that chromium appears to be more concentrated at the surface of the metal. This can be

explained by non-uniformities in the solid solution due to the manufacturing process or by surface composition alterations due to the presence of silica deposition.

From the data in the tables, the atomic ratio of oxygen to silicon (O:Si) versus deposition for all 6 cases can be seen graphically in Figure 26. Weight percentage is also graphed. The O:Si at.% ratio ranges from 1.35 to 2, whereby it is determined that the empirical formula is SiO_x where $1.35 \leq x \leq 2.0$. O:Si wt% ratio by comparison are in expected agreement. The ideal atomic ratio is 2 since the obtained nanosilica is SiO_2. It can be noted that the atomic ratio values for cases 1 (10μm) and 5 (60.3μm) are substantially lower than the expected value of 2, which means that there are less oxygen atoms than expected. A corresponding drop in weight percent is also noted for these cases. Some factors that could possibly influence the element amounts include variation in density from case to case, entrapment or void of gases within the interstitial pores, or chemical changes due to oxidation.

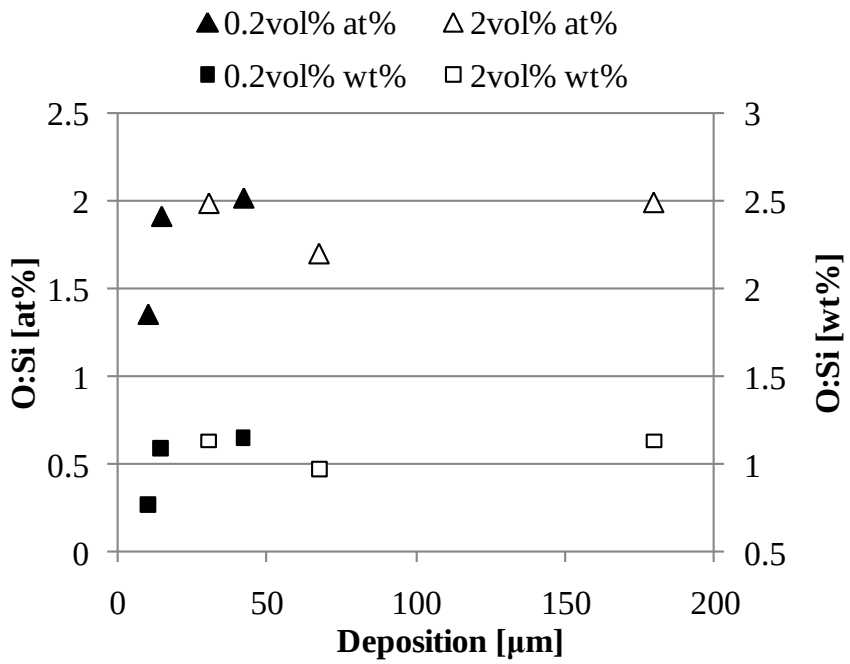

Figure 26: Oxygen to silicon ratios (at.% and wt.%) versus deposition for 0.2vol% and 2vol% silica.

Figure 27 graphically depicts the atom and weight percentages of oxygen and silicon independently for both 0.2vol% and 2vol% silica experiments versus the deposition amount for each case. As previously mentioned, in case 4, the electron beam penetrated through the entire 30µm deposition, and Figure 27a shows that it measured 21at.% silicon. In case 5 (60.3µm), with double the layer thickness, the beam passes through to approximately the top surface of the metal and measures 31at.% silicon. Lastly, in case 6 (180µm), which has more than double the deposition of case 5, there is an unexpected decrease in silicon in at.% (Figure 27a) and wt.% (Figure 27b), while oxygen remains approximately the same. A similar, albeit not as pronounced, trend occurs from case 2 (14µm) to case 3 (42µm), where the deposition is more than double in the latter case, but there is slight increase in silicon atom percent, while oxygen increases significantly more. Considering this occurrence and the density inferences discussed

previously, while the depth of the electron beam in case 6 is uncertain, it is possible to conclude that the average density of the silica deposition in case 6 is relatively less than that of the smaller deposition in cases 4 and 5. Similarly, it is possible to conclude that the average density of case 3 is relatively less compared with the thinner deposition of cases 1 and 2. This would imply that as heat flux increases and deposition increases towards burnout in an experimental run, the average density of the added height decreases, possibly suggesting a more loosely-packed outer layer, which is consistent with the inference of higher rate of deposition in the high heat flux region. In summary, it is possible that the percent increase of oxygen relative to that of silicon could be due to the entrapment of oxygen in larger interstitial pores formed by the less dense outer layer characteristic of higher heat fluxes.

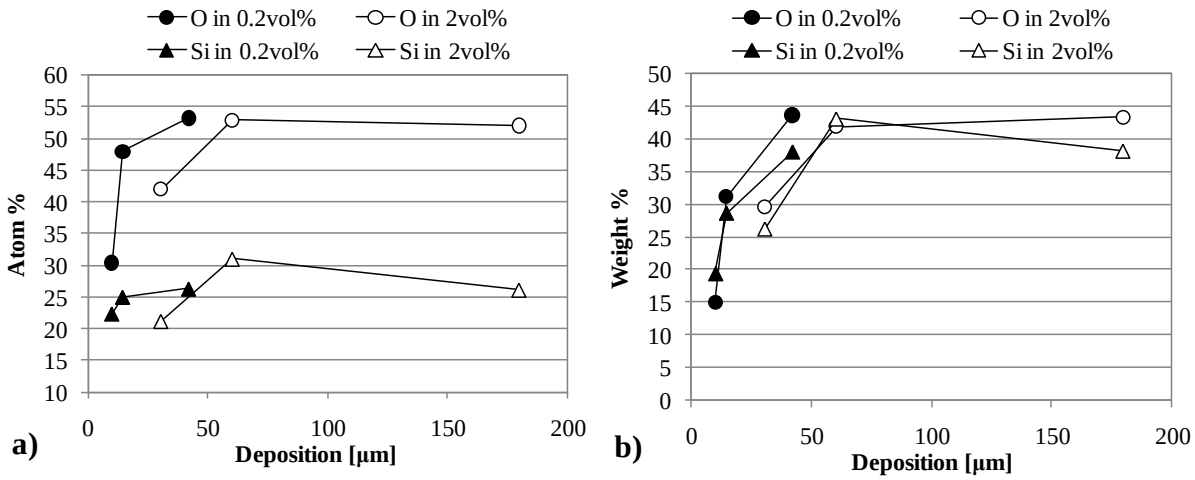

Figure 27: Oxygen and silicon individual percentage amounts versus deposition for 0.2vol% and 2vol% silica, a) atom percent, b) weight percent.

CHAPTER FIVE: CONCLUSIONS AND FUTURE WORK

- This study has shown a maximum CHF enhancement of up to 340% in 10-nm silica pool boiling experiments for ribbon heaters for particle concentrations less than 0.5vol%.
- The relationship of CHF with respect to nanoparticle concentration has been found to be non-monotonic with a peak around 0.2vol% to 0.4vol% for ribbon and wire heaters.
- Deposition was observed for all concentrations with a general upward trend. High heat transfer through inter-agglomerate pores and the highly wettable nature of the nanosilica are thought to be the main factors in CHF enhancement, with declining effect as deposition increases, lending itself to a detrimental thermal resistance effect.
- Results showed significant increase in viscosity for higher nanoparticle concentrations – up to ~40% higher than DI water for 2vol% silica concentration – which may also contribute to the effective decrease of CHF as particle concentration increases.
- Observations through flow visualization showed a presence of small bubbles and an increased bubble number density for higher concentrations, which were attributed to increased porosity and higher nucleation site density of the deposition layer as concentration was increased.
- Concentrations greater than 1vol% showed a large difference between the CHF and BHF deposition heights, and it was inferred that the 2vol% concentration coating had higher porosity and rate of deposition compared with 0.2vol% case.
- It was deduced that higher temperatures and heat fluxes of the pool boiling experiment accelerate the rate of deposition, with possibly the outermost layers being more porous.

- Results showed that pure water pool boiling CHF and BHF decrease with increasing surface area, and for similar surface areas, the wire has a 25% higher CHF than that of the ribbon heater.

Further research should be done by isolating the discussed parameters in this work to completely understand the effect of the surface characteristics and working fluid on the hydrodynamics and mechanisms that govern pool boiling. Regarding the nanofluid, surface chemistry of the particles should be further investigated to assess the hydration of the particles and lyophilic/ lyophobic characteristics of the nanofluid at various concentrations that may alter accordingly the wettability of the fluid. Furthermore, different diameter silica particles should be tested to investigate how size influences the aforementioned parameters and ultimately affects CHF enhancement. Initial data has been collected for 20nm silica and can be found in Appendix F. Additional work is needed to thoroughly characterize the deposition layer to fully illuminate its influence on nucleation site density, surface energy, and pool boiling hydrodynamics. A preliminary study is presented in Appendix G concerning the influence of deposition alone on CHF enhancement. Further analysis of this parameter could give tremendous insight into the mechanism of CHF enhancement.

APPENDIX A: OXIDE CONCENTRATION SAMPLE CALCULATIONS

$\rho_{oxide} := 2.25 \frac{g}{cm^3}$ Density of Silica

$\rho_{sol} := 1.1 \frac{g}{cm^3}$ Density of manufacturer-obtained solution (15% concentration)

$\varphi_{oxide} := 0.15$ wt/wt% Concentration of Silica in the water-based solution

$V_{H2O} := 160mL$ Input DI water volume

$\varphi_{final} := 2\%$ vol% Target Concentration

Equation 5 is used for concentration calculations for specified target volume percent concentrations. A Mathcad solve block is used for iterative solution-finding technique given an initial guess value in order to arrive at the solution. The solver for this block is a linear solver.

$Vsol := 10mL$ Guess for numerical calculation

Mathcad Solve Block

Given

$$\frac{\rho_{sol}}{\rho_{oxide}} \cdot \varphi_{oxide} \cdot Vsol = \varphi_{final} \cdot (V_{H2O} + Vsol) \quad (5)$$

$V_{sol} := Find(Vsol)$

Volume of oxide solution to be added:

$$V_{sol} = 60 \cdot mL$$

APPENDIX B: CHF CORRELATION COMPARISON FOR RIBBONS

ORIGIN ≡ 1 $i := 1..4$

Water Properties at 100°C (1 bar): boiling point: 100°C at 1 bar

$\rho_l := 958.3$	kg/m^3	Liquid Density
$\rho_v := 0.597$	kg/m^3	Vapor Density
$h_{lv} := 2256.700$	kJ/kg	Latent Heat of Vaporization
$\sigma := 0.05891$	N/m	Surface Tension
$g := 9.81$	m/s^2	Gravitational Acceleration

Present work's average CHF and BHF data in DI water for 4 horizontal ribbons of varied widths W, oriented horizontally.

Data:

$CHF_i :=$	$BHF_i :=$		$W_i :=$	
736	1218	kW/m^2	.0004	m
657	988		.00079	
717	735		.00159	
575	656		.00238	

Equation 6 is the capillary length scale L_b derived from the dimensionless Bond number, which relates the body forces to the surface tension forces.

$$L_b := \sqrt{\frac{\sigma}{g \cdot (\rho_l - \rho_v)}} \tag{6}$$

$$L_b = 2.504 \times 10^{-3} \text{ m}$$

Equations 7 and 8 are the present work's correlations for CHF and BHF ratios for horizontally-oriented ribbons, which were derived by iteration based on the original data points. They are dimensionless quantities based on a characteristic length.

$$qCHFratio := 0.53 \left(\frac{W}{L_b}\right)^{\frac{-1}{8}} \tag{7}$$

$$qBHFratio := 0.6 \left(\frac{W}{L_b}\right)^{\frac{-1}{3}} \tag{8}$$

Equation 9 is the Zuber [3] correlation for Maximum Heat Flux (CHF), and it provides the Max Heat Flux in kW/m^2 for water in these calculations based on an idealized flat plate and Helmholtz instability theory.

$$qmaxZ := 0.131 \cdot \rho_v \cdot h_{lv} \cdot \left[\frac{\sigma \cdot (\rho_l - \rho_v) \cdot g}{\rho_v^2} \right]^{\frac{1}{4}} \tag{9}$$

$$qmaxZ = 1.108 \times 10^3 \quad kW/m^2$$

The following is a verification of the present work's CHF correlation incorporating the Zuber Max Heat Flux correlation as outlined in [40] in order to accurately fit the original data values.

$$qmax := qmaxZ \cdot qCHFratio$$

$$qmax = \begin{pmatrix} 738.505 \\ 678.278 \\ 621.493 \\ 590.934 \end{pmatrix} \quad kW/m^2$$

Equations 10 and 11 are Lienhard and Dhir [40] CHF correlations for vertically-oriented ribbons with one side insulated and both sides heated, respectively. These correlations incorporate the Zuber Max Heat Flux correlation.

$$qratio1 := 1.4 \cdot \left(\frac{W}{L_b} \right)^{\frac{-1}{4}} \quad \text{one side insulated} \tag{10}$$

$$qratio2 := 1.18 \left(\frac{W}{L_b} \right)^{\frac{-1}{4}} \quad \text{both sides heated} \tag{11}$$

$$bhf := \frac{BHF}{qmaxZ} \quad \text{nondimensional BHF data}$$

$$chf := \frac{CHF}{qmaxZ} \quad \text{nondimensional CHF data}$$

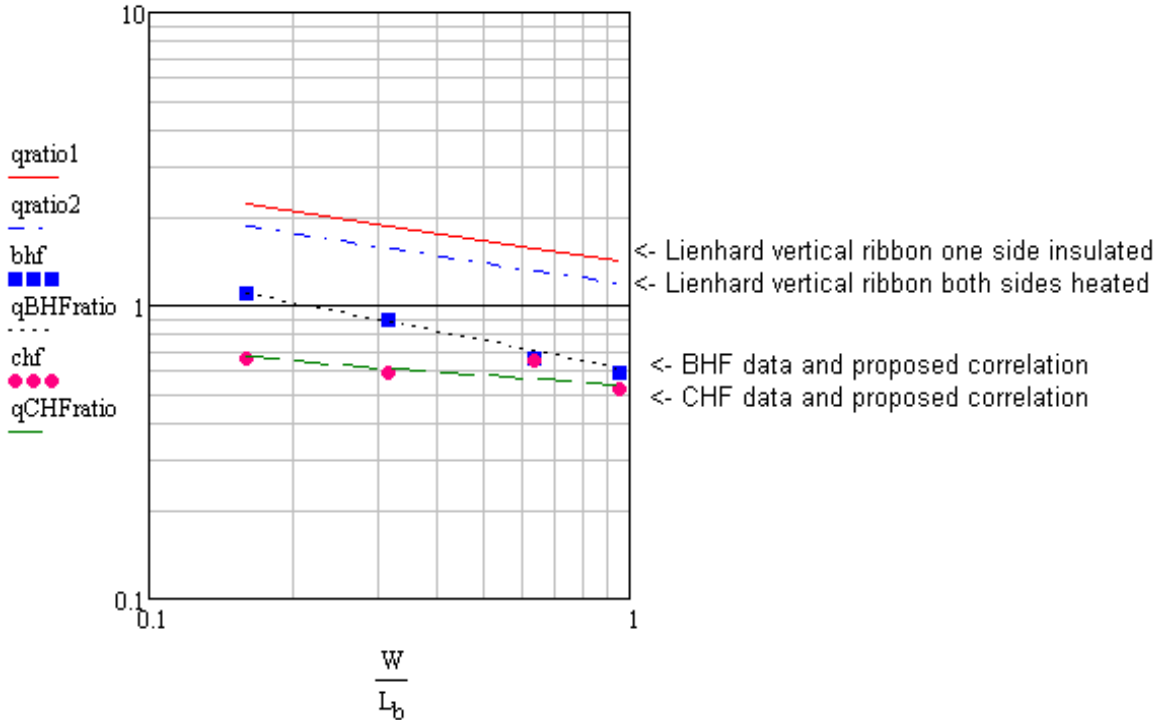

Range of applicability for proposed correlations (range of data set):

$$\frac{W}{L_b} = \begin{pmatrix} 0.16 \\ 0.315 \\ 0.635 \\ 0.95 \end{pmatrix}$$

Range of applicability $0.16 < W/L_b < 0.95$

APPENDIX C: WALL TEMPERATURE VERIFICATION CALCULATIONS

Equation 12 is the Stephan-Abdelsalam [41] correlation for wall temperature corresponding to the CHF condition for pool boiling of water.

$$q_{flux} = \left[C_1 \cdot (Tw - Tsat(P_1))\right]^{\frac{1}{0.327}} \qquad (12)$$

where $C_1 = 3.5$

$Tsat := 100\ °C$ Saturation Temperature of Water at ambient pressure

Mathcad Solve Block $Tw := 140\ °C$ Initial Guess

Given

$$657000 = [3.5 \cdot (Tw - Tsat)]^{\frac{1}{0.327}}$$

$Twall := Find(Tw)$

The Wall Temperature corresponding to the CHF condition is calculated to be

$\boxed{Twall = 123}$ °C

APPENDIX D: DEPOSITION PERCENTAGE SAMPLE CALCULATIONS

Shown in Figure 28 is a schematic of the rectangular ribbon with deposition and is a reference for the dimensions used for deposition sample calculations.

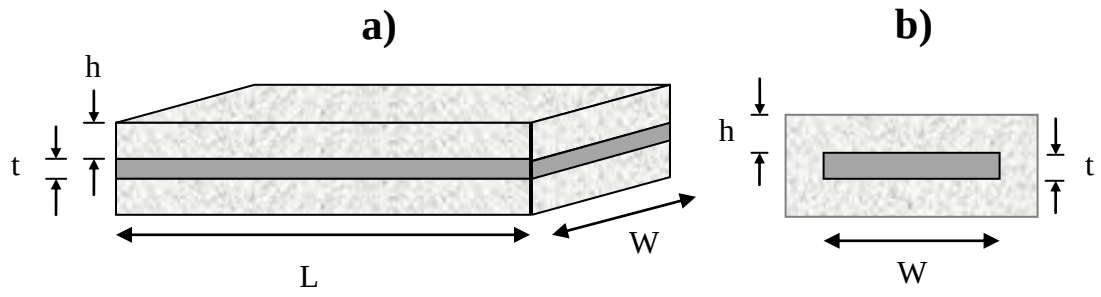

Figure 28: Schematic of nichrome ribbon with idealized deposition formation, a) isometric view of longitudinal cross-section, b) transverse cross-section.

The following are dimensions used for deposition calculations.

$L := 0.05m$	Length of Nichrome ribbon
$h := 195 \cdot 10^{-6} m$	Thickest deposition for the 2vol% silica concentration: Worst Case Scenario
$W := 0.00079m$	Width of Nichrome ribbon
$t := 0.000127m$	Thickness of Nichrome ribbon

Equation 13 was used to determine the volume occupied by deposition assuming uniform deposition height around entire ribbon as depicted in the transverse cross-section schematic.

$$Vol_{depo} := (2 \cdot h + t) \cdot (2 \cdot h + W) \cdot L - L \cdot W \cdot t \tag{13}$$

$$Vol_{depo} = 2.549 \times 10^{-8} \cdot m^3$$

Equation 14 was used to determine the mass in grams of deposited Silica.

$$M_{depo} := Vol_{depo} \cdot \rho_{oxide} \tag{14}$$

$$M_{depo} = 0.057 \cdot g$$

The total volume of silica + DI water nanofluid is

$$V_{total} := V_{H2O} + V_{sol}$$

$$V_{total} = 0.22\,L$$

Total mass (g) of Silica particles in the nanofluid is calculated via Equation 15.

$$M_{nf} := V_{total} \cdot \varphi_{final} \cdot \rho_{oxide} \tag{15}$$

$$M_{nf} = 9.9 \cdot g$$

Dividing the value obtained from Equation 14 by the value obtained from Equation 15, the weight of nanoparticles deposited on the ribbon as a percentage of the weight of nanoparticles in the fluid is calculated to be

$$\boxed{\frac{M_{depo}}{M_{nf}} = 0.58 \cdot \%}$$

APPENDIX E: FLOW VISUALIZATION

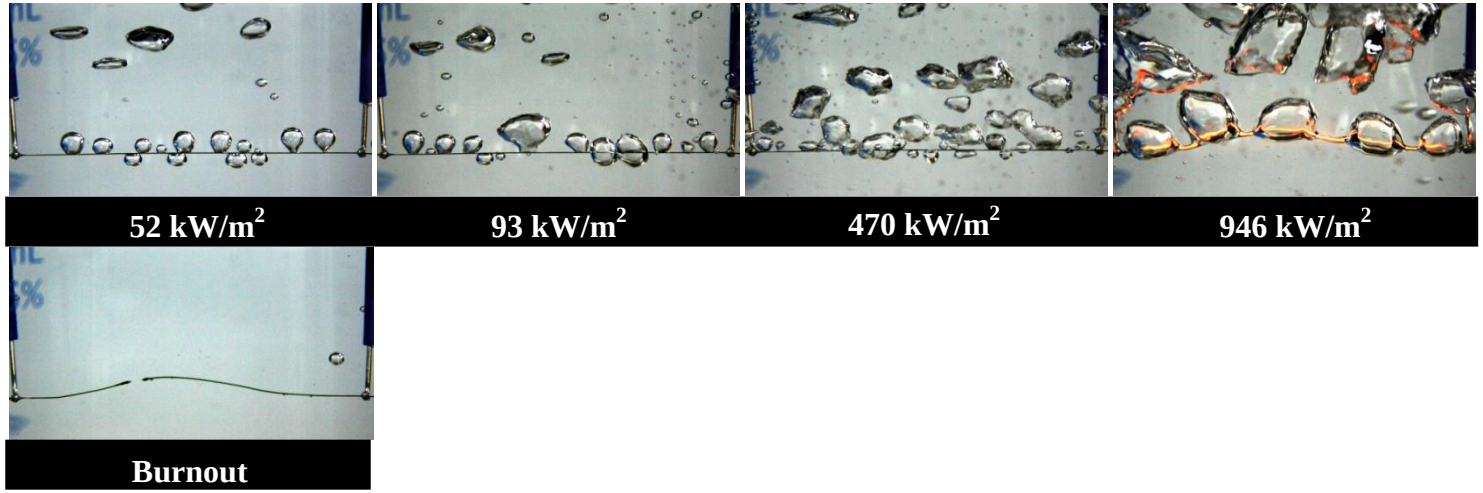

Figure 29: Flow visualization of pure DI water boiling using 0.79mm x 0.127mm nichrome ribbon shown for increasing heat flux values.

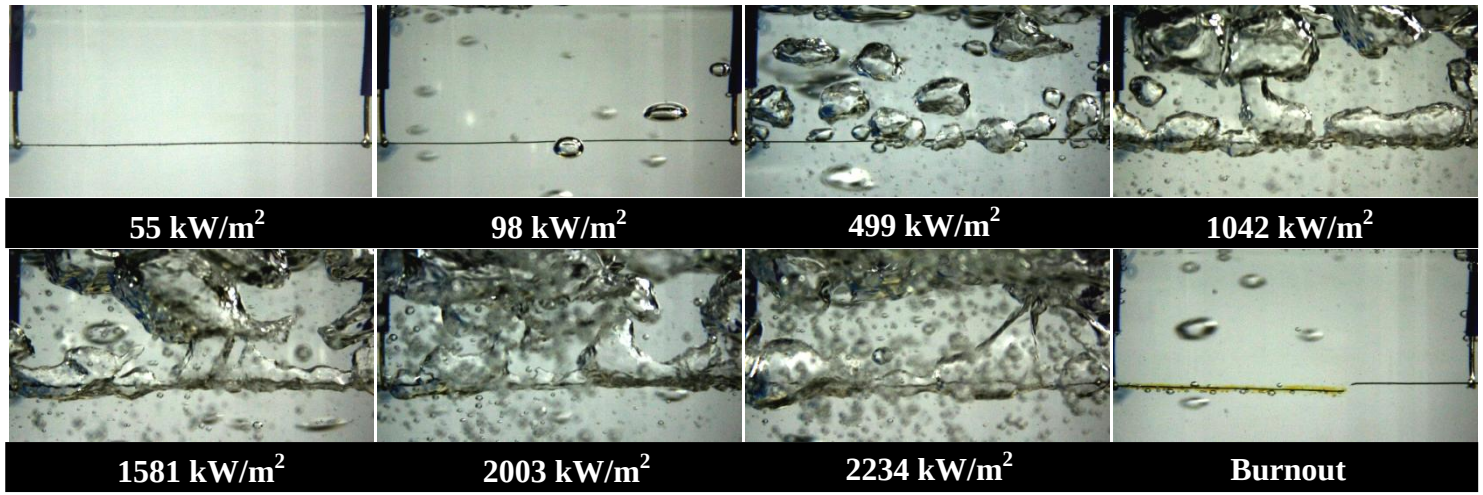

Figure 30: Flow visualization of 0.1vol% silica boiling using 0.79mm x 0.127mm nichrome ribbon shown for increasing heat flux values.

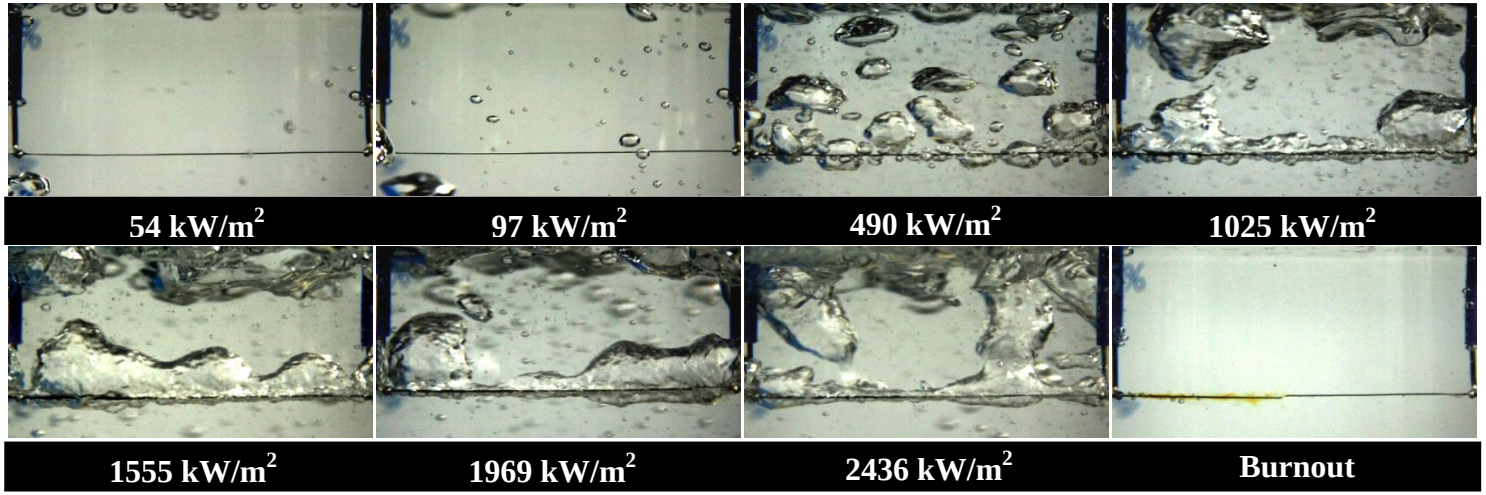

Figure 31: Flow visualization of 0.2vol% silica boiling using 0.79mm x 0.127mm nichrome ribbon shown for increasing heat flux values.

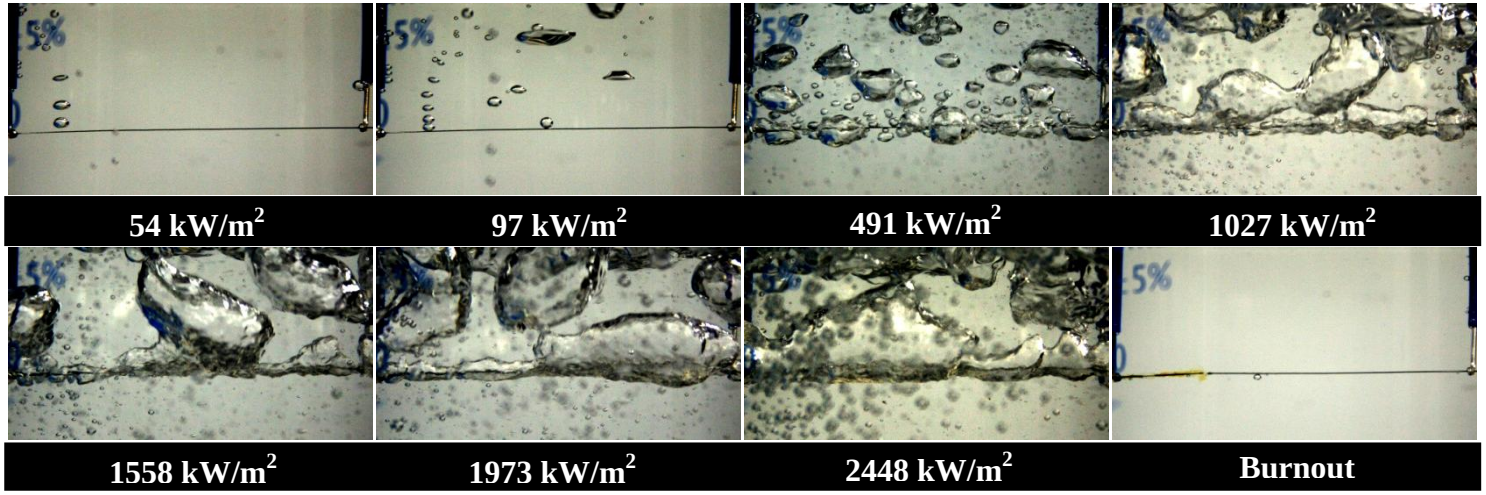

Figure 32: Flow visualization of 0.3vol% silica boiling using 0.79mm x 0.127mm nichrome ribbon shown for increasing heat flux values.

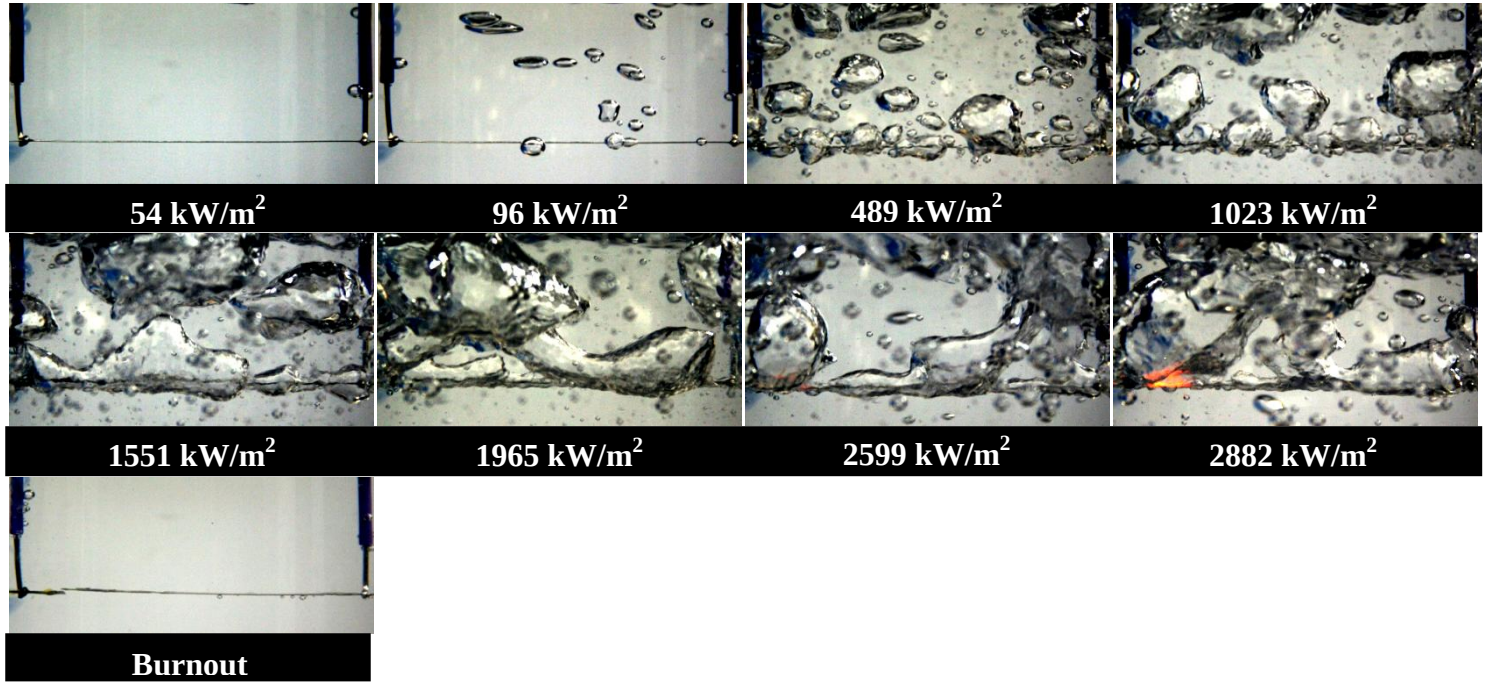

Figure 33: Flow visualization of 0.4vol% silica boiling using 0.79mm x 0.127mm nichrome ribbon shown for increasing heat flux values.

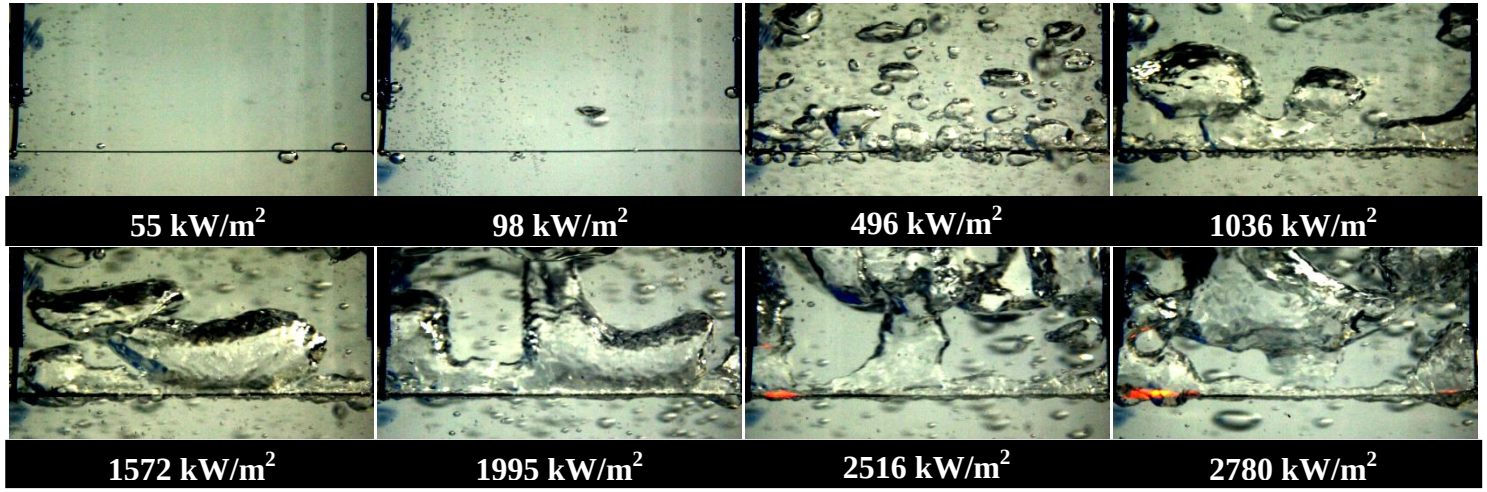

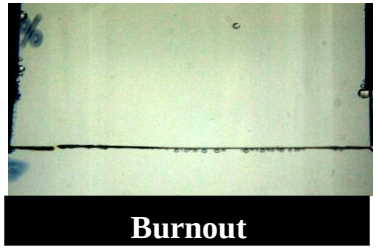

Figure 34: Flow visualization of 0.5vol% silica boiling using 0.79mm x 0.127mm nichrome ribbon shown for increasing heat flux values.

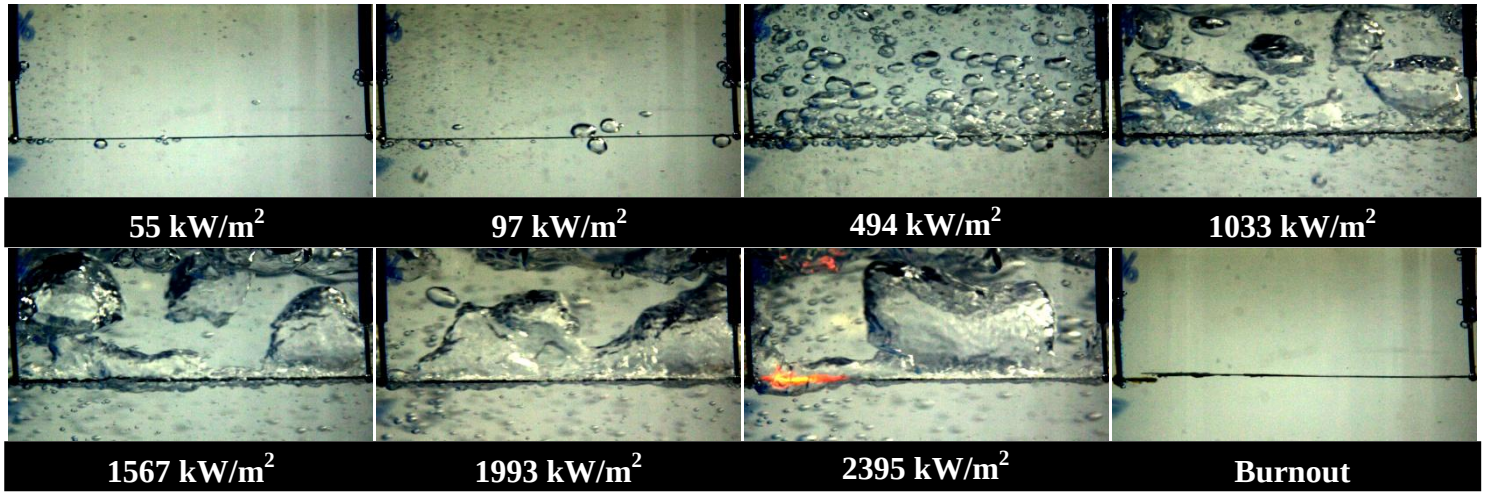

Figure 35: Flow visualization of 1vol% silica boiling using 0.79mm x 0.127mm nichrome ribbon shown for increasing heat flux values.

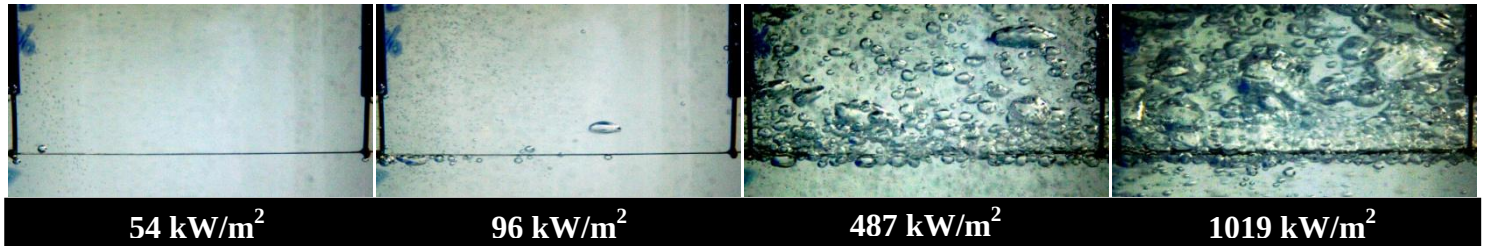

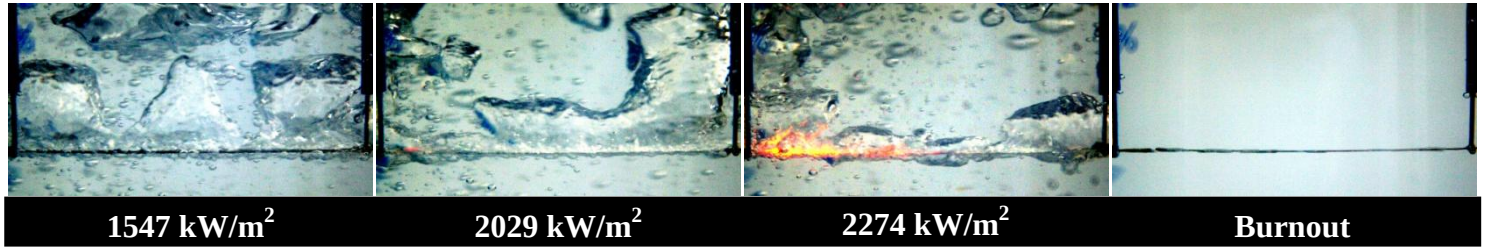

Figure 36: Flow visualization of 1.5vol% silica boiling using 0.79mm x 0.127mm nichrome ribbon shown for increasing heat flux values.

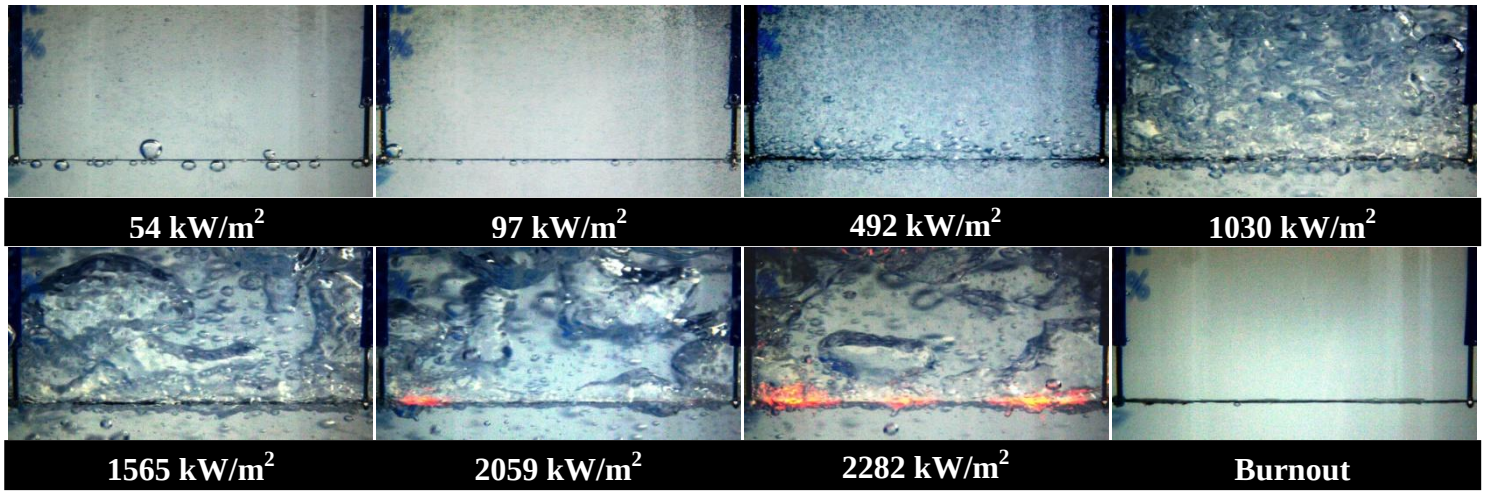

Figure 37: Flow visualization of 2vol% silica boiling using 0.79mm x 0.127mm nichrome ribbon shown for increasing heat flux values.

APPENDIX F: 20 NANOMETER SILICA DATA

Additional nanofluid pool boiling experiments have been done with 20nm silica particles at various concentrations with 0.79mm x 0.127mm ribbon, as a preliminary study of the heat transfer effects of a larger diameter particle. Figure 38 depicts the CHF and BHF enhancements over pure water versus increasing concentrations of 20nm silica nanofluid. Maximum CHF and BHF enhancements of 265% and 140%, respectively, have been found for 0.5vol% 20nm silica concentration. Preliminary results show a slight peak in the CHF and BHF enhancement versus particle concentration; however, more data are needed to establish a definite trend since the heat flux margin is relatively small.

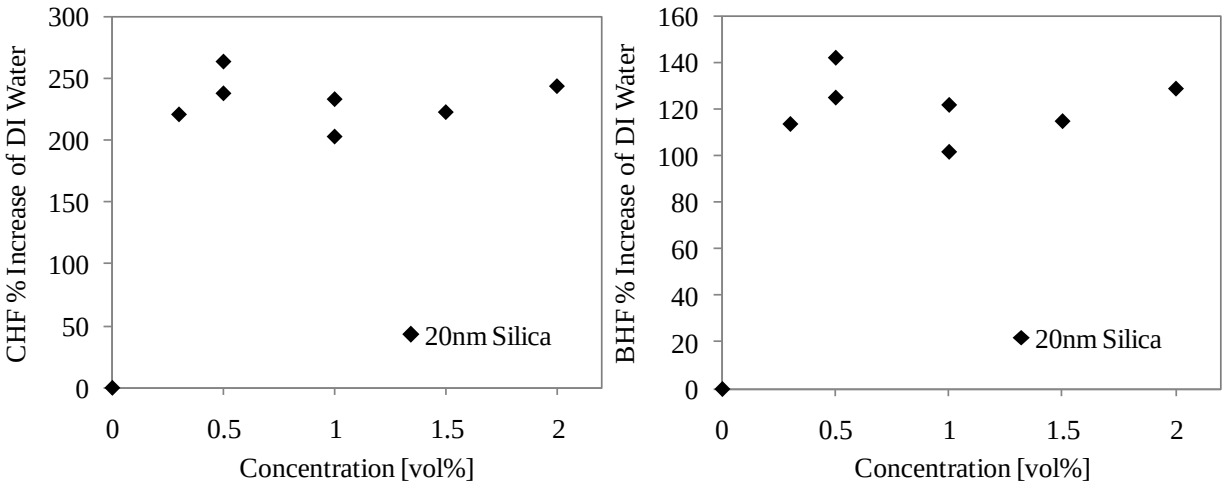

Figure 38: a) CHF and b) BHF percentage increase over DI water versus concentration of 20nm silica, 0.79mm x 0.127mm ribbon.

Figure 39 shows the dynamic viscosity ratio of 20nm silica to pure water. The viscosity increases significantly up to 28% for a small concentration of 0.3vol% and increases more gradually thereafter. Additionally, the average deposition height at BHF for 20nm silica on 0.79mm x 0.127mm ribbon is shown in Figure 40, where the error bars indicate the standard deviation of 5 measured locations along the ribbon. A maximum average deposition height of

~35μm was found for the range of concentrations tested. Further work and analysis are needed to exactly determine the compound influence these parameters have on CHF enhancement of 20nm silica pool boiling.

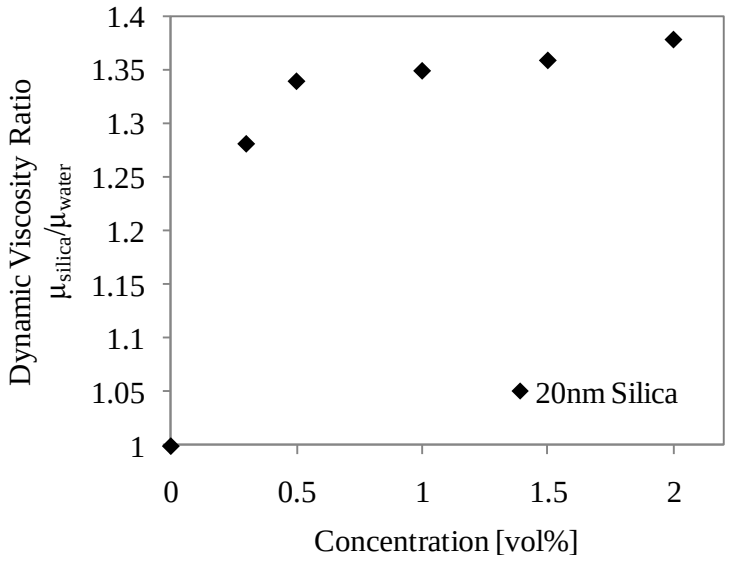

Figure 39: Dynamic viscosity of 20nm silica nanofluid at room temperature.

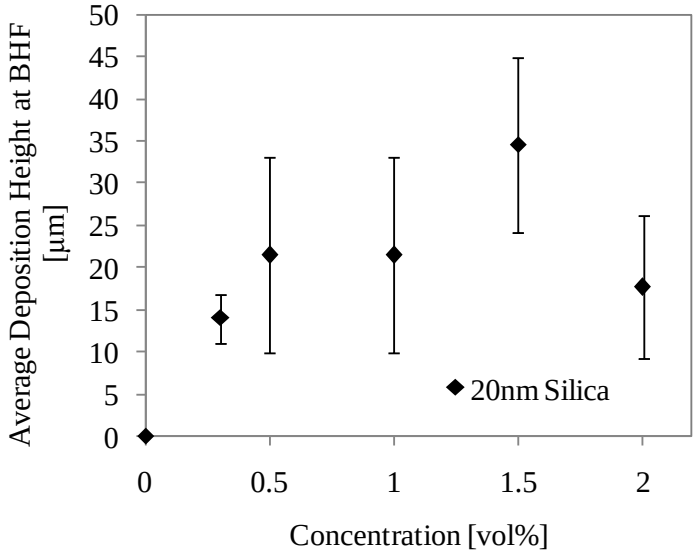

Figure 40: Average deposition heights at BHF versus 20nm-particle concentration.

APPENDIX G: WATER POOL BOILING USING SILICA-DEPOSITED SURFACE

A preliminary investigation has been done by boiling a nanoparticle-coated surface in DI water to see the effect of solely the deposition layer on CHF and BHF. Coating of the nichrome surface was achieved by boiling the 0.79mm x 0.127mm ribbon in nanofluid at increasing increments of electric current up to a certain value prior to the experiment with DI water. Two scenarios were posed for coating the surface with nanoparticles. The first scenario entailed applying low heat to the ribbon in high concentration 2vol% 10nm-silica. The second scenario involved applying high heat to the ribbon in low concentration 0.4vol% 10nm-silica. Both scenarios resulted in deposition heights between 15μm and 30μm. In the first scenario, the applied heat fluxes for coating purposes were 267 kW/m^2 and 297 kW/m^2, which are shown in Figure 41, and a CHF enhancement of up to 140% was found solely attributed to the deposition layer. In the second scenario, the applied heat flux pre-water boiling was 2208 kW/m^2, and the CHF enhancement was found to be approximately 275%, which is also attributed to the deposition. This significant increase from 140% can perhaps be explained by a consideration of the deposition characteristics such as microstructure. It was observed that the deposition for the second scenario had uniform texture, while that for the first scenario had more agglomerates. It is thought that a more consistent texture can allow for smaller bubble departure radius evenly spread along the surface and can further extend the CHF in the high heat flux region. It was reported in this work that this size ribbon showed a maximum CHF enhancement of 300% in nanofluid of 0.2vol% to 0.4vol%, and the foregoing results give credence to the hypothesis that deposition is a major factor in CHF enhancement. Further work is necessary to investigate the surface morphology and how that relates to the hydrodynamics of bubble formation and to validate these findings.

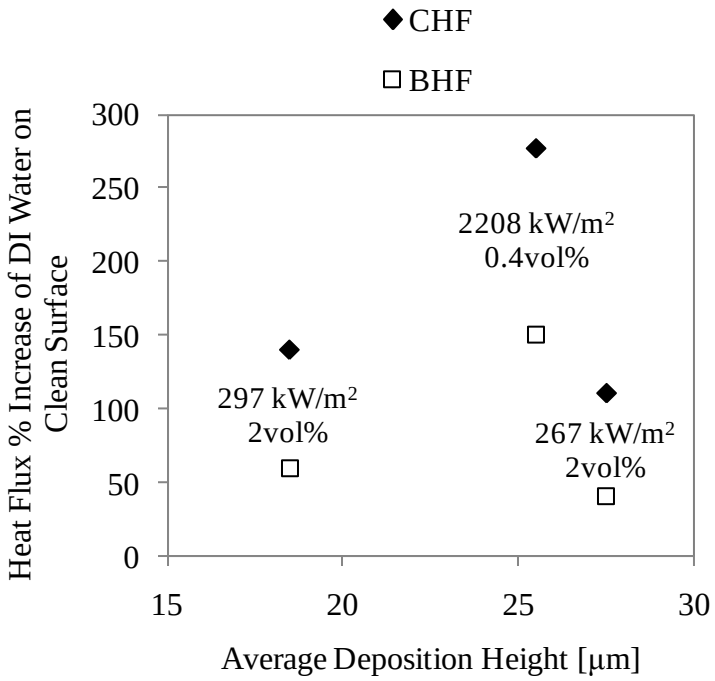

Figure 41: CHF and BHF percentage increase of water boiling on nanoparticle-deposited nichrome surface over water boiling on clean surface versus deposition height; values inside graph indicate the pre-water experiment conditions used to achieve nanoparticle coating.

The flow visualization is depicted in Figure 42 showing a comparison between water boiling of a clean nichrome surface and the two scenarios of silica-deposited surfaces. The rows show different values of heat fluxes, and the bottom-most picture in each column represents the moment just before burnout. In the low heat flux range, the pictures for the deposited surfaces show numerous small bubbles, forming a cloud of bubbles. In the higher heat flux range the large bubbles bear resemblance to those that were seen in nanofluid pool boiling (Figure 12). It is interesting to observe that the hydrodynamics of water boiling of a deposited surface appear to be quite similar macroscopically to that of the nanofluid pool boiling.

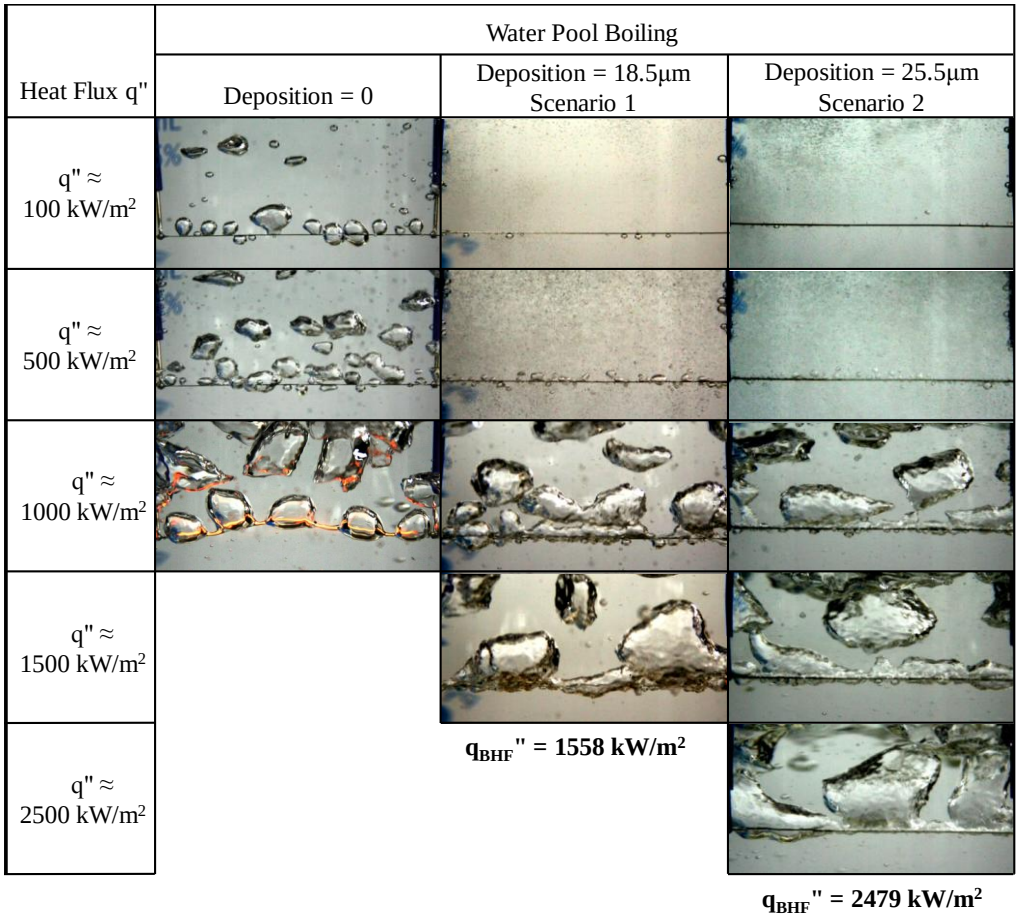

Figure 42: Flow visualization of water pool boiling with silica-deposited surfaces, 0.79mm x 0.127mm ribbon; Scenario 1 coating method – low heat flux in 2vol% 10nm-silica; Scenario 2 – high heat flux in 0.4vol% 10nm-silica.

REFERENCES

[1] S. Lee, S.U.-S. Choi, S. Li, J.A. Eastman, “Measuring thermal conductivity of fluids containing oxide nanoparticles,” J. Heat Transfer, vol. 121, May 1999, pp. 280–289.

[2] S. Nukiyama, “The maximum and minimum values of the heat Q transmitted from metal to boiling water under atmospheric pressure,” J. Japan Soc. Mech. Eng., vol. 37, 1934, pp. 367–374 (translated in Int. J. Heat Mass Transfer, vol. 9, 1966, pp. 1419–1433.

[3] N. Zuber, “Hydrodynamic aspects of boiling heat transfer,” AEC Report AECU-4439, June 1959.

[4] T.G. Theofanous, T.N. Dinh, J.P. Tu and A.T. Dinh, "The boiling crisis phenomenon: Part II: dryout dynamics and burnout," Exp. Therm. Fluid Sci., vol. 26, Aug. 2002, pp. 793–810.

[5] Y. Haramura and Y. Katto, “A new hydrodynamic model of the critical heat flux, applicable widely to both pool and forced convective boiling on submerged bodies in saturated liquids,” Int. J. Heat Mass Transfer, vol. 26, 1983, pp. 389–399.

[6] P. Vassallo, R. Kumar and S. D’Amico, “Pool boiling heat transfer experiments in silica–water nano-fluids,” Int. J. Heat Mass Transfer, vol. 47, Jan. 2004, pp. 407–411.

[7] D. Milanova and R. Kumar, “Role of ions in pool boiling heat transfer of pure and silica nanofluids,” Appl. Phys. Lett., vol. 87, 2005, pp. 233107-1–233107-3.

[8] H. Kim, J. Kim and M.H. Kim, “Effect of nanoparticles on CHF enhancement in pool boiling of nano-fluids,” Int. J. Heat Mass Transfer, vol. 49, Dec. 2006, pp. 5070–5074.

[9] S.M. You, J.H. Kim and K.H. Kim, “Effect of nanoparticles on critical heat flux of water in pool boiling heat transfer,” Appl. Phys. Lett., vol. 83, Oct. 2003, pp. 3374–3376.

[10] I.C. Bang and S. Heung Chang, “Boiling heat transfer performance and phenomena of Al2O3–water nano-fluids from a plain surface in a pool,” Int. J. Heat Mass Transfer, vol. 48, June 2005, pp. 2407–2419.

[11] S.J. Kim, I.C. Bang, J. Buongiorno and L.W. Hu, “Surface wettability change during pool boiling of nanofluids and its effect on critical heat flux,” Int. J. Heat Mass Transfer, vol. 50, Sept. 2007, pp. 4105–4116.

[12] W. Wu, H. Bostanci, L.C. Chow, Y. Hong, M. Su, J.P. Kizito, “Nucleate boiling heat transfer enhancement for water and FC-72 on titanium oxide and silicon oxide surfaces,” Int. J. Heat Mass Transfer, vol. 53, 2010, pp. 1773–1777.

[13] J.H. Lienhard, A heat transfer textbook, Englewood Cliffs, NJ: Prentice-Hall, 1987, pp. 404–438.

[14] H. Gjerkes and I. Golobic, “Pool boiling CHF on a laser heated thin plate,” Int. J. Heat Mass Transfer, vol. 43, June 2000, pp. 1999–2008.

[15] F. Tachibana, M. Akiyama and H. Kawamura, “Non-hydrodynamic aspects of pool boiling burnout,” J. Nucl. Sci. Tech., vol. 4, no. 3, pp. 121–130.

[16] I. Golobic and A.E. Bergles, “Effects of heater-side factors on the saturated pool boiling critical heat flux, ” Exp.Therm. Fluid Sci., vol. 15, July 1997, pp. 43–51.

[17] J.Y. Chang and S.M. You, “Enhanced boiling heat transfer from microporous surfaces: effects of a coating composition and method,” Int. J. Heat Mass Transfer, vol. 40, Dec. 1997, pp. 4449–4460.

[18] H.D. Kim and M.H. Kim, “Effect of nanoparticle deposition on capillary wicking that influences the critical heat flux in nanofluids,” Appl. Phys. Lett., vol. 91, July 2007, pp. 014104-1–014104-3.

[19] E. Forrest, E. Williamson, J. Buongiorno, L.-W. Hu, M. Rubner, R. Cohen, “Augmentation of nucleate boiling heat transfer and critical heat flux using nanoparticle thin-film coatings,” Int. J. Heat Mass Transfer, vol. 53, 2010, pp. 58–67.

[20] D. Wen and Y. Ding, “Experimental investigation into the pool boiling heat transfer of aqueous based gamma alumina nanofluids,” J. Nanoparticle Res., vol. 7, June 2005, pp. 265–274.

[21] S.K. Das, N. Putra and W. Roetzel, “Pool boiling characteristics of nano-fluids,” Int. J. Heat Mass Transfer, vol. 46, Feb. 2003, pp. 851–862.

[22] S. Kim, H.D. Kim, H. Kim, H.S. Ahn, H. Jo, J. Kim, M.H. Kim, “Effects of nano-fluid and surfaces with nano structure on the increase of CHF,” Exp. Thermal Fluid Sci., vol. 34, 2010, pp. 487–495.

[23] R.N. Wenzel, “Surface roughness and contact angle,” J. Phys. Colloid Chem., vol. 53, 1949, pp. 1466–1467.

[24] H.D. Kim, J. Kim and M.H. Kim, “Experimental studies on CHF characteristics of nano-fluids at pool boiling,” Int. J. Multiphase Flow, vol. 33, July 2007, pp. 691–706.

[25] S.P. Liaw, V.K. Dhir, “Effect of surface wettability on transition boiling heat transfer from a vertical surface,” Proceedings of the Eighth International Heat Transfer Conference, San Francisco, CA, vol. 4, 1986, pp. 2031–2036.

[26] J.S. Coursey and J. Kim, “Nanofluid boiling: The effect of surface wettability,” Int. J. Heat Fluid Flow, vol. 29, Dec. 2008, pp. 1577–1585.

[27] Z. Liu and L. Liao, “Sorption and agglutination phenomenon of nanofluids on a plain heating surface during pool boiling,” Int. J. Heat Mass Transfer, vol. 51, May 2008, pp. 2593–2602.

[28] Yu. A. Kirichenko and P.S. Chernyakov, “Determination of the first critical thermal heat flux on flat heaters,” J. Eng. Phys. Thermophys., vol. 20, 1971, pp. 699–702.

[29] S.G. Liter and M. Kaviany, “Pool-boiling CHF enhancement by modulated porous-layer coating: theory and experiment,” Int. J. Heat Mass Transfer, vol. 44, Nov. 2001, pp. 4287–4311.

[30] J. Buongiorno et al., “A benchmark study on the thermal conductivity of nanofluids,” J. Appl. Phys., vol. 106, 2009, pp. 094312-1–094312-14.

[31] R. Kumar and D. Milanova, “Dispersion and Surface Characteristics of Nano-Oxide Suspensions,” Ann. N.Y. Acad. Sci., vol. 1161, 2009, pp.472–483.

[32] Hyndman Industrial Products, Inc., Resistance wire heating data, www.resistancewire.com, 2009.

[33] W. Zhou and Z.L. Wang, Scanning microscopy for nanotechnology: techniques and applications, New York, NY: Springer, 2007.

[34] D. Milanova and R. Kumar, “Heat transfer behavior of silica nanoparticles in pool boiling experiment,” J. Heat Transfer, vol. 130, April 2008, pp. 042401-1–042401-6.

[35] H.E. Bergna and W.O. Roberts, Colloidal silica: fundamentals and applications, Boca Raton, FL: CRC Taylor & Francis, 2006, pp. 139.

[36] D. Wen, “Mechanisms of thermal nanofluids on enhanced critical heat flux (CHF),” Int. J. Heat Mass Transfer, vol. 51, Sept. 2008, pp. 4958–4965.

[37] D. Wasan and A. Nikolov, “Spreading of nanofluids on solids,” Nature, vol. 423, 2003, pp. 156–159.

[38] G.-S. Hwang and M. Kaviany, “Critical heat flux in thin, uniform particle coatings,” Int. J. Heat Mass Transfer, vol. 49, Mar. 2006, pp. 844–849.

[39] J.R. Thome, Enhanced Boiling Heat Transfer, Hemisphere, New York, 1990.

[40] J.H. Lienhard and V.K. Dhir, “Hydrodynamic prediction of peak pool-boiling heat fluxes from finite bodies,” J. Heat Transfer, vol. 95, 1973, pp. 152–158.

[41] K. Stephan and M. Abdelsalam, “Heat-transfer correlations for natural convection boiling,” Int. J. Heat and Mass Transfer, vol. 23, 1980, pp. 73–87.